Research Square

Preprints are preliminary reports that have not undergone peer review.
They should not be considered conclusive, used to inform clinical practice,
or referenced by the media as validated information.

Novel α-Microspheres Potentiate Radioembolization for Liver Cancer via Synergistic Vascular Disruption and Self-Powered Cerenkov Photodynamic Therapy

Weiwei Su
Naval Medical Center
Qifan Xu
Xuzhou Medical University
Yuqiao Wang
the First Affiliated Hospital of Naval Medical University
Tongyao Hu
the First Affiliated Hospital of Naval Medical University
Wenjie Li
the First Affiliated Hospital of Naval Medical University
Jiaojiao Li
Chinese Academy of Sciences
Jinming Tian
the First Affiliated Hospital of Naval Medical University
Chao Cheng
the First Affiliated Hospital of Naval Medical University
Yelin Wu
Shanghai East Hospital, School of Medicine, Tongji University
Xiao Li
the First Affiliated Hospital of Naval Medical University
Tao Wang
the First Affiliated Hospital of Naval Medical University
Changjing Zuo
cjzuo@smmu.edu.cn

Xuzhou Medical University

Research Article

Keywords: Transarterial radioembolization (TARE), 223Ra, Cerenkov radiation, Radio-microspheres, PET/CT imaging, Liver tumor

Posted Date: November 18th, 2026

DOI: https://doi.org/10.21203/rs.3.rs-11636697/v1

License: This work is licensed under a Creative Commons Attribution 4.0 International License.
Read Full License

Additional Declarations: No competing interests reported.

Abstract

Transarterial radioembolization (TARE) with β-emitting microspheres such as ^{90}Y serves as standard palliative care for advanced hepatocellular carcinoma (HCC), yet embolism-triggered intratumoral hypoxia confers radioresistance and limits therapeutic efficacy. Unlike β-rays, α-particles possess ultra-high linear energy transfer (LET) and oxygen-independent cytotoxicity, allowing efficient elimination of hypoxic tumor cells. Herein, we fabricated α-emitting ^{223}Ra-labeled chitosan/calcium phosphate microspheres (denoted ^{223}Ra-Chi/CaP MS). Capitalizing on the potent hypoxia-insensitive cytotoxicity of α-particles, these microspheres eradicate perivascular tumor cells and disrupt tumor vascular endothelium. To further eliminate tumor cells located distally from the vasculature, the microspheres were loaded with the photosensitizer methylene blue (MB) to harness Cerenkov photons emitted from the ^{223}Ra decay chain and achieve Cerenkov radiation-induced photodynamic therapy (CR-PDT), thereby expanding the therapeutic reach. The resulting ^{223}Ra-Chi/CaP-MB MS exhibited excellent physicochemical stability, sustained MB release, and prolonged tumor retention following hepatic artery delivery. *In vitro* studies demonstrated that the synergistic action of ^{223}Ra and CR-PDT triggered extensive DNA double-strand breaks and robust ROS generation, leading to enhanced apoptosis even under hypoxic conditions. In a rat orthotopic liver tumor model, TARE using ^{223}Ra-Chi/CaP-MB MS exerted more potent tumor growth inhibition than embolization controls or plain ^{223}Ra-Chi/CaP MS, predominantly through disrupting tumor blood vessels, blocking compensatory angiogenesis, and triggering extensive tumor cell apoptosis. With confirmed biosafety, this ^{223}Ra-based microsphere platform represents a transformative strategy to revitalize TARE for β-refractory liver cancer.

Introduction

Hepatocellular carcinoma (HCC), which accounts for nearly 90% of all primary liver malignancies, ranks as the sixth most prevalent cancer and the third leading cause of cancer-related mortality worldwide [1]. A substantial proportion of HCC patients are diagnosed at the intermediate or advanced stages, when curative surgical resection is no longer feasible. In this context, transarterial radioembolization (TARE) employing microspheres radiolabeled with β-emitting radionuclides, particularly the clinically established ^{90}Y resin and glass microspheres, yields significant therapeutic outcomes for patients with intermediate to advanced HCC [2, 3]. By integrating the ischemic and hypoxic effects resulting from tumor feeding artery embolization with the cytotoxicity induced by localized β-rays internal irradiation, TARE exhibits superior disease control and an improved safety profile. However, despite its clinical promise, the efficacy of TARE is often limited by the hypoxic tumor microenvironment (TME) resulting from the embolization itself [4, 5]. TARE-derived intratumoral hypoxia induces ischemic necrosis in HCC cells, but the resulting hypoxic TME elicits powerful prosurvival adaptive responses in residual tumor cells. For example, hypoxia stabilizes hypoxia-inducible factor-1α (HIF-1α) and increases its intracellular accumulation. Stabilized HIF-1α further initiates a cascade of downstream signaling pathways that promote angiogenesis, metabolic reprogramming, and upregulation of DNA damage repair machinery; collectively, these molecular alterations confer resistance to β-emitting radiation [6, 7]. Existing studies

on novel microspheres have predominantly centered on the development of β-emitting radioactive microspheres, or fabricating drug-loaded microspheres to potentiate the therapeutic efficacy of TARE [8–10]. Nevertheless, the intrinsic radiobiological properties of β-rays hinder these approaches from adequately resolving hypoxia-driven radioresistance. Consequently, designing novel microspheres that combine localized radionuclide delivery with targeted abrogation of hypoxia-driven adaptive defenses represents a core strategy to resolve the therapeutic bottlenecks associated with β-microsphere TARE.

Distinguished from β-rays, α-particles exhibit an extremely high linear energy transfer (LET), with α-particles averaging 50–200 keV/μm versus just 0.1–0.5 keV/μm for β-rays [11, 12]. This unique physicochemical profile enables α-particles to induce irreparable, clustered DNA double-strand breaks (DSBs) via direct ionization effect [13]. As a result, the cytotoxicity of α-particles remains largely independent of the oxygen enhancement ratio, making them uniquely effective against hypoxic tumor cells that typically exhibit resistance to β-rays. Clinical evidence demonstrates that targeted α-emitting radiopharmaceuticals (such as ^{225}Ac and ^{223}Ra) produce stronger antitumor activity than β-emitting radionuclide agents (e.g., ^{177}Lu), and remain therapeutically active in tumors resistant to β-radiation [14]. In light of this, α-emitting radionuclides exhibit remarkable potential to surmount hypoxia-mediated radioresistance, rendering them a more favorable option than β-emitters for HCC TARE. However, the application of TARE with α-microspheres is not without limitations. First, the primary limitation of α-particles lies in their minimal tissue penetration range (45–100 μm, equivalent to the diameter of 5–10 cells), such that their cytotoxic effects are confined solely to proximal tumor cells [15]. Predictably, post-embolization α-particle irradiation induces profound injury to the vascular endothelium of tumor-feeding hepatic vessels, but this radiation only exerts potent cytotoxicity on tumor cells—including hypoxic subpopulations immediately surrounding blood vessels. Without a cross-fire effect, α-particles fail to eliminate liver tumor cells located deep within tumor tissue far from the vasculature. Second, the large ionic radii inherent to α-emitting radionuclides complicate the development of robust chelators, making it difficult to prevent radionuclide *in vivo* dissociation and the subsequent risk of off-target toxicity [16]. Hence, resolving the aforementioned two limitations is a prerequisite for achieving efficacious therapeutic implementation of TARE with α-microspheres for liver cancer.

In this study, we leveraged the α-emitting radionuclide ^{223}Ra to fabricate a novel chitosan/calcium phosphate microsphere (^{223}Ra-Chi/CaP MS) platform. Capitalizing on the chemical homology between Ra^{2+} and Ca^{2+}, we successfully embedded ^{223}Ra within the Chi/CaP crystal lattice through ion exchange, yielding ^{223}Ra-Chi/CaP MS with outstanding structural stability. To overcome the intrinsically short cytotoxic range of α-particles, we further encapsulated the photosensitizer methylene blue (MB) into the microspheres. The Cerenkov radiation (CR) emitted during the decay cascade of ^{223}Ra was utilized to initiate CR-induced photodynamic therapy (CR-PDT) [17]. Distinct from conventional external light-triggered PDT, the internally generated CR circumvents the penetration depth limitation of exogenous light sources [18]. Moreover, MB-sensitized CR-PDT proceeds through both Type I and Type II photodynamic pathways. Notably, its oxygen-independent Type I radical reactions sustain potent tumoricidal effect against tumor cells, rendering this combinatorial modality well-adapted to the hypoxic

TME following TARE. As such, when applied for TARE in a rat liver cancer model, the fabricated ^{223}Ra-Chi/CaP-MB MS not only eliminate perivascular liver tumor cells efficiently—including hypoxia-induced radioresistant subpopulations—and aggravate tumor vasculature damage, but also eradicate distal tumor cells via CR-PDT, thereby achieving superior therapeutic outcomes (Fig. 1). Collectively, our engineered α-microsphere platform effectively surmounts embolization-induced hypoxia while simultaneously potentiating antitumor efficacy, offering a transformative strategy for liver cancer refractory to conventional β-microsphere TARE.

Methods

Materials and reagents

Chitosan powder, calcium nitrate tetrahydrate ($Ca(NO_3)_2{\cdot}4H_2O$), ammonium dihydrogen phosphate ($NH_4H_2PO_4$), glacial acetic acid, paraformaldehyde (PFA) fixative, and Trizol lysis buffer were all purchased from Shanghai Aladdin Biochemical Technology Co., Ltd. $^{223}RaCl_2$ solution was provided by Bayer Healthcare Co., Ltd. Methylene blue (MB) was obtained from Sigma Corporation. Aminophenyl fluorescein (APF) was purchased from AAT Bioquest. Phosphate-buffered saline (PBS), Dulbecco's modified Eagle medium with high-glucose (DMEM), penicillin–streptomycin double antibiotic, trypsin, fetal bovine serum (FBS), cell counting kit-8 (CCK-8), Annexin V-fluorescein isothiocyanate/propidium iodide (Annexin V-FITC/PI) apoptosis detection kit, reactive oxygen species (ROS) assay kit, Calcein-AM/propidium iodide (Calcein-AM/PI) staining kit, cell cycle detection kit, and TRIeasy total RNA extraction reagent were supplied by Shanghai Yeasen Biotech Co., Ltd. Isoflurane was acquired from Qingdao Oubofang Pharmaceutical Technology Co., Ltd. Penicillin injection and dexamethasone sodium phosphate (DSP) injection were obtained from Hebei Yuanzheng Hemu Pharmaceutical Co., Ltd. and Shanxi Ruicheng Kelong Veterinary Pharmaceutical Co., Ltd., respectively. Fluorine-18 fluorodeoxyglucose (^{18}F-FDG) was obtained from Shanghai Atom Kexing Pharmaceutical Co., Ltd. Anti-γ-H2AX primary antibody was purchased from Dojindo Laboratories. 4% paraformaldehyde, anti-CDKN1A, anti-PDGFR-β, anti-CD31, anti-CD105, anti-VEGFA, anti-β-actin primary antibodies, and corresponding secondary antibodies were supplied by Wuhan Sanying Biotechnology Co., Ltd. All reagents were used as received without further purification. The N1S1 rat hepatocellular carcinoma cell lines were purchased from Shanghai Ze Ye Biotech Co., Ltd. Specific pathogen-free (SPF)-grade Wistar rats were obtained from Beijing SiPeiFu Biotechnology Co., Ltd.

Preparation of chitosan calcium phosphate microspheres (Chi/CaP MS)

Chitosan/calcium phosphate microspheres (Chi/CaP MS) were synthesized according to a previously published report [19]. Briefly, 3 g chitosan powder was dispersed in 300 mL of 0.33% (w/v) aqueous acetic acid under continuous magnetic stirring for 24 h to complete full dissolution, yielding a

homogeneous chitosan stock solution. In parallel, 11.8 g $Ca(NO_3)_2 \cdot 4H_2O$ (0.05 mol) and 3.45 g $NH_4H_2PO_4$ (0.03 mol) were separately dissolved in 50 mL distilled water to prepare calcium and phosphate precursor solutions, respectively. All three precursor solutions were preheated simultaneously in a 70°C water bath for 1 h. Afterwards, the three solutions were fully blended and incubated at 70°C under constant heating for 30 min to complete the mineralization reaction. After reaction termination, the mixed suspension was centrifuged at 5000 r/min for 5 min to harvest the Chi/CaP MS precipitate. The collected microspheres were rinsed three times with distilled water and re-suspended in PBS for refrigerated storage at 4°C prior to use.

Radiolabeling of Chi/CaP MS with Ra

Radium (Ra) shares identical main group positioning with calcium (Ca) and barium (Ba) in the periodic table, conferring highly similar chemical properties that support an element substitution strategy for efficient ^{223}Ra radiolabeling. Prior to formal labeling, non-radioactive Ba^{2+} were used as stable surrogates to optimize reaction conditions and verify substitution feasibility. Briefly, 0.5 mL of Chi/CaP MS suspension was mixed with 0.1 mL of 0.01 mol/L $BaCl_2$ solution. After 24 h of constant-temperature shaking incubation, the mixture was centrifuged at 5000 rpm for 5 min, and the harvested precipitate was designated as Ba-Chi/CaP MS.

For formal radiolabeling, 10 μCi of $^{223}RaCl_2$ solution was mixed homogenously with 0.5 mL of Chi/CaP MS suspension and incubated with continuous shaking for 24 h. The mixture was then centrifuged at 5000 rpm for 5 min, and the resulting ^{223}Ra-Chi/CaP MS precipitate was resuspended in sterile physiological saline for subsequent experiments. SPECT/CT imaging was employed to quantitatively determine the radiolabeling efficiency of ^{223}Ra-Chi/CaP MS. Equal aliquots of ^{223}Ra-Chi/CaP MS suspension and $^{223}RaCl_2$ solution were incubated at room temperature for 12 h before SPECT/CT scanning. Free $^{223}RaCl_2$ solution exhibited uniform radioactive signals, whereas ^{223}Ra-Chi/CaP MS showed concentrated radioactivity at the tube bottom due to sedimentation. Manually delineated regions of interest (ROIs) were used to record radioactive counts for the calculation of radiolabeling efficiency.

The *in vitro* stability of ^{223}Ra-Chi/CaP MS was evaluated via 7-day continuous incubation in PBS. Following incubation and centrifugation, repeated SPECT/CT scanning was performed to validate radiotracer retention and microsphere structural stability. A prolonged incubation assay was conducted to investigate the structural durability of ^{223}Ra-Chi/CaP MS during radionuclide decay and the impact of long-term α-particle self-irradiation on microsphere morphology. Based on the 11.4-day half-life of ^{223}Ra, microspheres were incubated in PBS for 5 half-lives (approximately 57 days) to achieve sufficient radionuclide decay and sustained self-irradiation. Finally, scanning electron microscopy (SEM) was utilized to characterize microsphere microstructure and clarify the effects of long-term α-irradiation and nuclide decay on structural integrity.

Characterization of Chi/CaP MS

The micro-morphology and elemental distribution of the microspheres were characterized via SEM combined with energy-dispersive X-ray spectroscopy (EDS). All samples were immobilized on conductive adhesive and sputter-coated with gold using a Quorum SC7620 sputter coater (10 mA, 45 s) before imaging. SEM morphological observation was performed at an accelerating voltage of 3 kV with a SE2 secondary electron detector, while EDS elemental mapping of Ba-Chi/CaP MS was acquired at 15 kV. The specific surface area of Chi/CaP MS was measured using a Micromeritics ASAP 2460 analyzer based on nitrogen adsorption–desorption isotherms at 77 K. Prior to measurement, samples were vacuum-degassed at 120°C for 6 h, and the specific surface area was calculated via the Brunauer–Emmett–Teller (BET) model. The crystalline phase composition of the microspheres was identified by X-ray diffraction (XRD) with Cu-Kα radiation, with a scanning 2θ range of 10°–80° and a scanning rate of 2 °/min. Surface chemical functional groups were analyzed by Fourier-transform infrared spectroscopy (FTIR) using the KBr pellet technique, and spectra were recorded over the wavenumber range of 4000–400 cm^{-1} at a resolution of 4 cm^{-1}. Furthermore, the thermal stability of the microspheres was assessed by thermogravimetric analysis (TGA) under a nitrogen atmosphere, where samples were heated from 30°C to 800°C at a constant heating rate of 10°C/min.

Methylene blue (MB) encapsulation and in vitro release kinetics

First, a standard calibration curve for methylene blue (MB) was established using serial aqueous MB concentrations ranging from 0.1 to 5.0 mg/L. For the drug loading assay, 1 mL of Chi/CaP MS suspension was blended with an equal volume of 5 mg/L MB solution in an Eppendorf tube, followed by continuous shaking incubation for 24 h. After centrifugation at 5000 rpm over 5 min, the absorbance of the collected supernatant was quantified at 664 nm via a UV-Vis spectrophotometer (Alpha-1500, Shanghai Puyuan Instrument Co., Ltd., China) to calculate the drug loading efficiency; the harvested precipitate was denoted Chi/CaP-MB MS. Subsequently, *in vitro* MB release experiments were performed by re-suspending Chi/CaP-MB MS in 10 mL PBS under constant shaking. At pre-set time intervals (1, 2, 4, 8, 12, 24, 48, 72, 120, and 138 h), 1 mL of release medium was sampled, and an equivalent volume of pre-warmed fresh PBS was replenished instantly to maintain a constant system volume. The MB concentration of each withdrawn sample was determined spectrophotometrically at 664 nm to generate cumulative drug release curves.

Cerenkov imaging and ROS detection of Ra-Chi/CaP-MB MS in solution

To detect ^{223}Ra-induced Cerenkov luminescence imaging, three aqueous samples were prepared in Eppendorf tubes: $^{223}RaCl_2$ (4 μCi), MB (8 μg/mL), and a mixture of $^{223}RaCl_2$ and MB pre-reacted for 10 min. Optical signals from each tube were captured via an in vivo imaging system (VISQUE Invivo Smart-

LF, Korea). Image acquisition was performed under full emission spectrum mode with the excitation channel blocked to exclusively record Cerenkov luminescence.

ROS production in four aqueous suspensions—pure water (blank control), Chi/CaP-MB MS, ^{223}Ra-Chi/CaP MS and ^{223}Ra-Chi/CaP-MB MS—was quantified with APF fluorescent probe. Briefly, 100 μL of each sample was dispensed into designated wells of a black 96-well plate, with five biological replicates allocated per group. An equal volume (100 μL) of APF working solution (5 μM) was added to each well and mixed homogeneously. The plate was incubated in dark at room temperature for 30 min, followed by an additional 1 h light-shielded reaction period. Fluorescence intensity was quantified on a multi-mode microplate reader with excitation set at 490 nm and emission at 515 nm. Relative ROS generation of each group was normalized to the blank group.

Cell culture

The N1S1 rat hepatocellular carcinoma cell line is widely adopted as an experimental model to recapitulate human HCC. N1S1 cells were cultured in high-glucose DMEM medium supplemented with 10% fetal bovine serum (FBS) and 1% penicillin–streptomycin mixture. Cell incubation was carried out in a constant temperature and humidity cell incubator (Thermo Scientific) maintained at 37°C with 5% CO_2 and 70%–80% relative humidity. The culture medium was refreshed every 48 h, and N1S1 cells in favorable proliferative conditions were harvested for subsequent cell experiments.

Cell viability and cytotoxicity analysis

Cell viability assays with the CCK-8 kit were conducted to assess the cytotoxic effects of Chi/CaP MS, MB and $^{223}RaCl_2$ on N1S1 cells, as well as to screen optimal working concentrations for subsequent cellular experiments. Briefly, N1S1 cells suspended in high-glucose DMEM were seeded into three separate 96-well plates at a density of 8×10^3 cells per well. Three concentration-gradient plates were arranged: the first plate contained serial concentration of Chi/CaP MS (0–2 mg/mL); the second plate contained serial concentrations of MB (0-128 μg/mL); the third plate contained serial radioactive concentration of $^{223}RaCl_2$ (0–4 μCi/mL), with five biological replicates per concentration. After a 24 h cell attachment phase in serum-free DMEM, the original culture supernatant was aspirated and replaced with DMEM containing two-fold serially diluted Chi/CaP MS, MB or $^{223}RaCl_2$, matching the corresponding treatment plate. After 24 h co-incubation with the test substances, 10 μL CCK-8 reagent was added to each well, and the plates were incubated in complete darkness for 3 h for color development. The absorbance of each well was recorded at 450 nm using a Multiskan FC microplate reader (Thermo Scientific, Waltham, MA, USA). Relative cell viability (%) was calculated as the absorbance ratio of treated groups to the untreated blank control group.

Calcein-AM/PI dual staining

N1S1 cells were seeded into 24-well plates at a density of 8×10^4 cells per well and cultured for 24 h to allow complete cell attachment. Afterwards, the culture medium was aspirated, and cells were randomly allocated to four groups: untreated control, MB alone (4 μg/mL), ^{223}Ra-Chi/CaP MS (2 μCi/mL), and ^{223}Ra-Chi/CaP-MB MS group. Following a 24 h incubation with the respective treatments, the culture supernatant was discarded, and cells were gently washed twice with pre-cold PBS. The Calcein-AM/PI double staining working solution was freshly prepared by fully blending 5 μL of 2 mM Calcein-AM stock solution and 15 μL of 1.5 mM PI stock solution into 5 mL 1× Assay Buffer. A volume of 0.5 mL staining solution was added to each well, and plates were incubated at 37°C for 15 min under light-shielded conditions. After incubation, cells were washed twice with PBS to remove residual unbound dye. Fluorescence imaging was performed using a fluorescence microscope (Nikon Eclipse CI, Tokyo, Japan) equipped with a 480 nm excitation filter for dual-channel synchronous detection. Live cells stained by Calcein-AM emitted green fluorescence (Ex/Em = 494/517 nm), whereas dead cells stained with PI displayed red fluorescence (Ex/Em = 535/617 nm).

Apoptosis analysis by flow cytometry

Consistent with the Calcein-AM/PI double staining experiment described above, N1S1 cells from all four groups (untreated control, MB alone, ^{223}Ra-Chi/CaP MS, and ^{223}Ra-Chi/CaP-MB MS) were harvested after 24 h of treatment. Cell pellets were resuspended in 100 μL binding buffer and co-stained with 5 μL Annexin V-FITC and 5 μL PI for 20 min in dark. An unstained untreated blank control and two single-color compensation control tubes (Annexin V-FITC single stain and PI single stain) were prepared in parallel for fluorescence compensation during flow cytometry acquisition. Afterwards, stained cells were rinsed and diluted with 200 μL PBS prior to data acquisition using an ImageStream mkII flow cytometer (MilliporeSigma, Burlington, MA, USA) equipped with IDEAS™ analysis software.

Detection of intracellular ROS by flow cytometry

In line with the apoptosis assays, N1S1 cells were collected following 24 h treatment and stained with 10 μM of DCFH-DA for 30 min in dark. An unstained, untreated cell sample was prepared in parallel as the blank control. To avoid cell sedimentation and clumping, cell suspensions were gently mixed by manual pipetting every 5 min during incubation. After staining, cells were rinsed twice with DMEM and resuspended in PBS. The intracellular green fluorescence intensity reflecting ROS levels was quantified via an ImageStream mkII flow cytometer (MilliporeSigma, Burlington, MA, USA).

Immunofluorescence analysis of γ-H2AX

For immunofluorescence staining of γ-H2AX, N1S1 cells were seeded onto coverslips placed in 24-well plates at a density of 8×10^4 cells per well and cultured overnight for attachment. Cells were then exposed to four different treatments: control, MB, ^{223}Ra-Chi/CaP MS, and ^{223}Ra-Chi/CaP-MB MS, with a total treatment duration of 24 h. After treatment, coverslip-grown cells were fixed with 4% paraformaldehyde for 10 minutes and thoroughly rinsed with PBS. Cells were permeabilized by incubation in 100 μL of 1% Triton X-100 (diluted in PBS) for 20 minutes. Following another PBS wash,

non-specific antigen binding was blocked by incubation with 3% BSA solution for 30 minutes at room temperature. After extensive PBS rinsing, cells were incubated overnight at 4°C with primary anti-phospho-H2AX antibody diluted 1:200 in PBS. Subsequently, samples were incubated with Alexa Fluor 488-conjugated goat anti-rabbit secondary IgG antibody (1:400 dilution) for 50 minutes in dark, followed by 10 min of DAPI nuclear counterstaining in dark. After a final series of PBS washes, the coverslips were mounted onto glass slides and visualized under a fluorescence microscope (Nikon Eclipse CI).

Evaluation of cytotoxicity under simulated hypoxia

To investigate the influence of oxygen tension on the cytotoxicity induced by α-particles and CR-PDT, parallel CCK-8 viability assays were performed under normoxic (21% O_2) and hypoxic (1% O_2) conditions. Briefly, N1S1 cells were seeded into 96-well plates at a density of 8×10^3 cells per well and cultured until fully adherent. Identical four groups were established in each oxygen environment with a total medium volume of 200 μL per well: untreated control, MB (4 μg/mL), ^{223}Ra-Chi/CaP MS (2 μCi/mL), and ^{223}Ra-Chi/CaP-MB MS. After 24 h of incubation under respective oxygen conditions, 10 μL of CCK-8 working solution was supplemented to each well, and plates were incubated in dark for 3 h. Absorbance values at 450 nm were recorded on a Multiskan FC microplate reader (Thermo Scientific, Waltham, MA, USA). The relative cell viability (%) was calculated using the formula described in the preceding section.

RNA-seq analysis

To dissect the underlying mechanisms through which combined ^{223}Ra irradiation and CR-PDT exert synergistic tumor cell killing, transcriptome profiling via RNA-seq was performed on treated N1S1 cells. For RNA-seq library construction and sequencing, N1S1 cells were seeded in 6-well plates and cultured in DMEM for 24 h to achieve complete attachment, with an initial seeding density of 5×10^5 cells suspended in 1 mL medium per well. Three biological replicate wells were prepared for each experimental group. After full cell adherence, the spent culture medium was aspirated and replaced with either fresh medium or medium containing ^{223}Ra-Chi/CaP-MB MS (2 μCi/mL of ^{223}Ra corresponding to 4 μg/mL of MB). Following a 24 h treatment period, cell pellets were collected, and total cellular RNA was isolated using TRIzol reagent according to the manufacturer's instructions. High-throughput RNA sequencing services were commissioned from Shanghai Majorbio Bio-pharm Technology Co., Ltd., and all downstream bioinformatics analyses were executed on the Majorbio Cloud Platform (www.majorbio.com).

Cell cycle distribution by flow cytometry

Matching the sample collection schedule for RNA-seq analysis, cells from the control and ^{223}Ra-Chi/CaP-MB MS groups were harvested at 24 h post-treatment. Cells were fixed in prechilled 70% ethanol at 4°C for 2 h and washed with PBS. The cell pellets were fully resuspended in 300 μL PI working solution (50 μg/mL) supplemented with 5 μL RNase A stock solution (100 μg/mL). After 30 min of incubation at room temperature in dark, samples were analyzed on an ImageStream mkII imaging flow cytometer (MilliporeSigma, Burlington, MA, USA).

Quantitative real-time reverse transcription PCR (qRT-PCR)

For qRT-PCR analysis, N1S1 cells from the control and ^{223}Ra-Chi/CaP-MB MS groups were collected, and total cellular RNA was isolated using 1 mL TRIzol Reagent. RNA concentration and purity were quantified with a NanoDrop 2000 spectrophotometer, while RNA integrity was verified on a Bioanalyzer, with an RNA integrity number (RIN) greater than 7 for all samples. Qualified RNA samples were normalized to a concentration of 20 ng/μL prior to reverse transcription.

A total volume of 20 μL reverse transcription reaction was formulated, consisting of 4 μL 5× SweScript All-in-One SuperMix for qPCR, 1 μL gDNA Remover, 10 μL diluted total RNA, and RNase-free water to reach the final volume. After thorough mixing and brief centrifugation, reverse transcription was carried out under a temperature gradient: 25°C for 5 min, 42°C for 30 min, and 85°C for 5 s to terminate the reaction. Custom specific primer pairs were redesigned to amplify mRNA transcripts of CDKN1A.

Each 15 μL qPCR amplification mixture comprised 7.5 μL 2× Universal Blue SYBR Green qPCR Master Mix, 1.5 μL pooled forward/reverse primers (2.5 μM), 2.0 μL template cDNA, and 4.0 μL nuclease-free water. Reaction mixtures were transferred into 0.1 mL PCR plates, which were then sealed and centrifuged to eliminate bubbles. The qPCR thermal profile was set as follows: an initial denaturation step at 95°C for 30 s; 40 amplification cycles of 95°C for 15 s and 60°C for 30 s; subsequent melting curve analysis ranging from 65°C to 95°C with a temperature increment of 0.5°C per step. Relative mRNA expression levels of target genes were normalized to the housekeeping gene GAPDH and calculated on a Bio-Rad CFX Connect real-time PCR detection system.

Western blotting

N1S1 cells from the control and ^{223}Ra-Chi/CaP-MB MS groups were harvested via centrifugation at 2000 rpm for 5 min. Cell pellets were resuspended in RIPA lysis buffer containing phosphatase inhibitors at a volume of 250 μL per 1 × 10^6 cells, followed by a 30-min incubation on ice for complete protein lysis. Lysates were then clarified by centrifugation at 12000 × g for 15 min at 4°C, and the resultant supernatants were retained as total whole-cell protein extracts. Protein lysates were denatured by mixing with 5× SDS loading buffer and heating at 95°C for 10 min. Denatured proteins were resolved via SDS-PAGE electrophoresis and transferred onto 0.45 μm PVDF membranes. To block non-specific antigen-antibody binding, membranes were incubated in 5% skim milk prepared in TBST buffer for 1 h at room temperature. Subsequently, membranes were probed overnight with primary antibody targeting CDKN1A; β-actin served as the internal loading control. After thorough washing with TBST, blots were incubated with HRP-conjugated secondary antibodies (dilution 1:5000) for 1 h at room temperature. Following multiple TBST rinses, protein bands were visualized using an ECL chemiluminescence reagent, and blot images were captured using an SCG-W30000 imaging scanner. Relative band densitometry was analyzed and quantified with AIWBwell™ software (Servicebio, Wuhan, China).

Establishment of liver tumor xenograft model in rats

Seven-week-old male Wistar rats were maintained under SPF housing conditions. Prior to orthotopic liver tumor implantation, rats were fasted for 24 h with water deprivation for 8 h. All surgical operations were conducted under inhalational isoflurane anesthesia (2% isoflurane balanced with oxygen at a flow rate of 800–1000 mL/min). Following laparotomy to fully expose the left hepatic lobe, 100 μL of cell suspension (1:1 volume mixture of PBS and Matrigel) containing 1×10^7 N1S1 cells were slowly injected into the liver parenchyma using a 1 mL insulin syringe. For postoperative care, each rat received intramuscular injections of penicillin (200,000 units) and dexamethasone once daily for three successive days. This regimen was implemented to prevent surgical infection and mitigate postoperative inflammatory response.

At 7 days after implantation, ^{18}F-FDG positron emission tomography/computed tomography (PET/CT) scanning was performed to evaluate tumor growth status. Rat models bearing liver tumors were eligible for further treatment groups only when they met all enrollment standards: maximal tumor diameter exceeding 1 cm, maximum standardized uptake value (SUVmax) ≥ 1.5, and no evidence of distant or intra-abdominal metastasis detected on PET/CT scans.

Transarterial radioembolization in rat liver tumor models

Eligible tumor-bearing rats were randomly assigned to four groups (n = 3 per group): sham embolization group (control), Chi/CaP MS group, ^{223}Ra-Chi/CaP MS group, and ^{223}Ra-Chi/CaP-MB MS group. All surgical procedures were conducted under isoflurane inhalation anesthesia. A 2-cm longitudinal incision was made slightly to the right of the abdominal midline to expose the common hepatic artery, proper hepatic artery, and gastroduodenal artery. The distal gastroduodenal artery was ligated, and the common hepatic artery was temporarily clamped for blood flow control. Subsequently, a micro arteriotomy involving approximately one-third of the vessel wall was created at the proximal segment of the ligated gastroduodenal artery. A guidewire-assisted catheter was inserted through the arteriotomy and advanced to the bifurcation of the proper hepatic artery, followed by guidewire removal. Vascular integrity was confirmed by sterile saline injection with no vascular leakage. Afterwards, 100 μL of corresponding formulations (saline, Chi/CaP MS, ^{223}Ra-Chi/CaP MS, or ^{223}Ra-Chi/CaP-MB MS, with the ^{223}Ra-containing groups dosed at 74 kBq of ^{223}Ra per rat) was slowly administered, and the catheter lumen was flushed with a small volume of saline to eliminate residual microspheres. Upon complete catheter withdrawal, the gastroduodenal artery was permanently ligated to terminate regional blood perfusion, and the abdominal incision was routinely sutured and closed.

^{223} Ra SPECT/CT imaging

To evaluate the *in vivo* retention and biodistribution of ^{223}Ra-Chi/CaP-MB MS, serial ^{223}Ra SPECT/CT imaging was conducted in tumor-bearing rats at 1, 5, 10 and 15 days after intra-arterial microsphere administration. All scans were performed on a dual-head SPECT/CT system (Symbia T16, Siemens Healthineers) equipped with high-energy and high-resolution collimators. SPECT imaging was acquired with the following parameters: 128 × 128 matrix, zoom factor of 1.45, 35 keV photopeak with a 20%

energy window, 60 s acquisition per frame, and 32 frames in total. Concurrent CT scanning was performed at a tube voltage of 130 kV and a tube current of 35 mA, with a pitch of 1.0 and a reconstructed slice thickness of 0.75 mm. For quantitative biodistribution analysis, three-dimensional regions of interest (ROIs) were manually delineated on co-registered SPECT/CT reconstructed images, encompassing orthotopic liver tumors and major normal tissues, including the heart, healthy liver, spleen, lungs, kidneys, stomach, intestines, urinary bladder, and skeletal muscle. The total radioactivity and volumetric values of individual ROIs were measured, and the biodistribution was calculated as the percentage injected dose per milliliter of tissue (%ID/mL).

^{18}F-FDG PET/CT imaging

To evaluate the therapeutic efficacy of TARE utilizing ^{223}Ra-microspheres against liver tumor, serial ^{18}F-FDG PET/CT scans were performed on a Biograph 64 PET/CT scanner (Siemens Healthineers). Imaging timepoints included 24 h before intervention (baseline), as well as days 7 and 15 post-treatment. Briefly, each liver tumor-bearing rat received tail vein injection of ^{18}F-FDG at a dose of 9 MBq/kg. After anesthesia induction, animals were positioned supine, and whole-body PET/CT acquisition was initiated 1 h following radiotracer administration.

PET acquisition was set to 3 min per bed position, and raw PET data were reconstructed via the ordered-subset expectation maximization (OSEM) algorithm. CT scanning parameters were configured as below: tube voltage, 100 kV; tube current, 150 mA; slice thickness, 0.6 mm; slice increment, 1 mm. CT images were reconstructed with a medium-smooth H40s kernel. All raw imaging datasets were imported into the MedEx post-processing platform for coregistration and image reconstruction. Three-dimensional ROIs were manually outlined covering the entire tumor lesion to determine the SUVmax. Tumor volume was calculated by measuring the longest and perpendicular diameters on the largest tumor cross-section of CT image, according to the formula: tumor volume = 0.5 × longest diameter × perpendicular diameter^2.

^{68}Ga-DOTA-RGD PET/CT imaging

As $\alpha_v\beta_3$ integrin exhibits prominent overexpression on tumor neovascular endothelial cells and can be selectively recognized by RGD motifs, ^{68}Ga-DOTA-RGD PET/CT serves as a reliable imaging tool to assess tumor angiogenesis [20]. We thus applied this imaging technique to evaluate intratumoral neovascularization status in liver tumors after α-microsphere-based TARE. $^{68}GaCl_3$ was eluted from a commercial ^{68}Ge/^{68}Ga generator with HCl (0.1 M), and subsequent radiolabeling of DOTA-RGD was carried out in accordance with our previously reported protocol [21]. For *in vivo* angiogenic PET/CT imaging, scans were acquired at 48 h after TARE intervention. Briefly, each liver tumor-bearing rat underwent tail vein injection of ^{68}Ga-DOTA-RGD at a radioactivity dose of approximately 7.4 MBq. Whole-body PET/CT acquisition was initiated 30 min following radiotracer administration on a Biograph 64 PET/CT scanner (Siemens Healthineers), whose intrinsic spatial resolution reached 1 mm. CT scanning was operated at a tube voltage of 120 kV and tube current of 35 mA, with reconstructed CT slices

processed on the TrueD workstation. Radiotracer uptake within tumor lesions was quantified by calculating the SUVmax.

Histological and immunofluorescence analysis of tumor tissues

At day 15 post-TARE, tumor-bearing rats were sacrificed, and tumor specimens were collected for multiple histological examinations. Hematoxylin-eosin (H&E) staining was conducted for general morphological observation; TdT-mediated dUTP nick end labeling (TUNEL) staining was used to detect tumor cell apoptosis, while Ki-67 immunohistochemistry was performed to assess the proliferative activity of liver tumor cells. Furthermore, immunofluorescence staining targeting cluster of differentiation 31 (CD31), CD105 and platelet-derived growth factor receptor β (PDGFR-β) was performed to investigate the anti-angiogenic effects of TARE using α-emitting microspheres. These three biomarkers serve as characteristic markers of intratumoral neovessel formation, proliferation and maturation, and their expression levels within tumor tissues harvested from all groups were quantitatively assessed.

Furthermore, to evaluate difference in the impacts of α-microsphere and β-microsphere-based TARE on tumor neovascularization, a supplementary cohort of liver tumor-bearing rats received TARE with ^{90}Y-labeled carbon microspheres (37 MBq per rat). Tumor samples were collected on day 15 post-TARE for vascular endothelial growth factor A (VEGFA) immunofluorescence staining.

Biosafety evaluation of TARE using ^{223}Ra-Chi/CaP-MB MS

To evaluate the biosafety of TARE with the novel α-emitting microspheres, peripheral blood samples were collected from tumor-bearing rats at day 15 post-TARE for complete blood count (CBC) and serum biochemical quantification of hepatic and renal function markers. In parallel, major visceral organs including the heart, pancreas, spleen, lungs, kidneys, stomach, small intestine, and colon were dissected from tumor-bearing rats across all groups, and all specimens underwent H&E staining for histopathological lesion examination.

Statistical analysis

All statistical analyses were conducted with GraphPad Prism 10.4 software. All quantitative data are expressed as mean ± standard deviation (SD). Two-tailed statistical tests were implemented for all comparisons, with a significance threshold set at $P < 0.05$. Comparisons of two independent groups relied on independent-samples *t*-test for normal, homoscedastic data; Welch's *t*-test was used for normal data with unequal variances, while non-normal data were analyzed with the Mann-Whitney U test. For multi-group comparisons, one-way ANOVA followed by Tukey's HSD post-hoc test was adopted for normally distributed data with homogeneous variance. Kruskal–Wallis test with Dunn's post-hoc test was used for non-normal data, and Welch ANOVA combined with Games-Howell test was applied for datasets with unequal variances.

Results and discussion

Synthesis and characterization of ^{223}Ra-Chi/CaP-MB MS

Given that radium (Ra) and calcium (Ca) occupy the same group in the periodic table and possess highly analogous chemical characteristics, synthesizing calcium-containing microspheres followed by subsequent ^{223}Ra radiolabeling has been validated as a reliable strategy to fabricate α-emitting radioactive microspheres [22, 23]. Herein, calcium-incorporated Chi/CaP MS were prepared in this study to serve as carriers for ^{223}Ra radiolabeling. As shown in the SEM image, the as-fabricated Chi/CaP MS exhibited a regular spherical morphology with abundant porous structures and an average particle diameter of 26.18 ± 2.04 μm (Fig. 2A). Barium (Ba), a stable nonradioactive analog of ^{223}Ra, was employed as a cold labeling agent to validate the feasibility of our elemental substitution radiolabeling strategy. The resulting Ba-loaded Chi/CaP MS preserved the morphological features identical to those of the pristine Chi/CaP MS (**Fig. S1**). EDS elemental mapping revealed a homogeneous distribution of Ba throughout the microsphere matrix, along with the intrinsic constituent elements Ca, P, C, and O (Fig. 2B). Quantitative elemental analysis further demonstrated that the measured Ba content was in good agreement with the theoretical loading dosage (**Table S1**), thereby confirming the validity of this ion-exchange labeling strategy.

XRD diffractograms were recorded to identify the crystalline phases of Chi/CaP MS (Fig. 2C), whereas FTIR spectroscopy verified the characteristic vibrational peaks corresponding to -OH, P-O and C-H bonds (Fig. 2D). TGA profiling demonstrated the outstanding thermal stability of the microspheres (**Fig. S2**). N_2 adsorption-desorption isotherms presented a typical H3-type hysteresis loop (Fig. 2E), indicative of porous frameworks constructed from stacked nanosheet building blocks. The BET specific surface area of Chi/CaP MS was calculated as 63.2649 m^2/g. Supplementary BJH pore size analysis demonstrated hierarchically distributed pores spanning 3.8–52 nm. The adsorption and desorption branches yielded specific surface areas of 49.8641 m^2/g and 80.5525 m^2/g, paired with pore volumes of 0.289942 cm^3/g and 0.145158 cm^3/g, respectively (Fig. 2F, **Table S2**). Collectively, the uniform pore size distribution and high porosity equip Chi/CaP MS with favorable structural properties to achieve high loading capacity of photosensitizer MB.

Inspired by the favorable outcomes of cold labeling, we further adopted this elemental substitution strategy to fabricate ^{223}Ra-Chi/CaP MS. SPECT/CT imaging showed homogeneous radioactive distribution in the $^{223}RaCl_2$ solution, while intense radioactive signals were predominantly localized within the precipitated sediment of the ^{223}Ra-Chi/CaP MS groups (Fig. 2G). Quantitative ROI analysis yielded an exceptional radiolabeling efficiency exceeding 99%. *In vitro* stability tests verified that the radiochemical purity of ^{223}Ra-Chi/CaP MS remained greater than 95% following 7 days of static incubation in PBS. Importantly, after prolonged incubation spanning five physical half-lives of ^{223}Ra (≈ 57 days) to simulate sustained long-term self-irradiation, the microspheres still maintained intact morphological structure (Fig. 2H). Taken together, these results validate the superior structural and

radiochemical stability of ^{223}Ra-Chi/CaP MS. Owing to the negligible structural erosion induced by α-particles emitted from ^{223}Ra, this microsphere holds great promise for subsequent *in vivo* TARE.

Furthermore, the CR derived from the ^{223}Ra decay chain serves as an excellent intrinsic light source for CR-PDT. Multiple investigations have highlighted the prominent advantages of employing radionuclide-derived CR (e.g., ^{18}F, ^{131}I, ^{68}Ga, ^{90}Y) as an endogenous light source for tumor PDT [24–27]. Upon loading the photosensitizer MB onto ^{223}Ra-Chi/CaP MS, the microspheres acquire CR-PDT activity. In aqueous solution, ^{223}Ra decay produces blue-colored Cerenkov light. After introduction of MB, MB absorbs this CR, leading to attenuation and even quenching of the blue-light signal (**Fig. S3**). Benefiting from the multi-porous architecture of Chi/CaP MS, MB was incorporated into the microspheres, and the resulting Chi/CaP-MB MS exhibited a desirable MB-loading capacity of 13.36 μg/mg. *In vitro* release curves acquired via UV–vis spectrophotometry verified sustained MB elution from Chi/CaP-MB MS, with the cumulative release fraction attaining 85% within 138 h (**Fig. S4**). This sustained MB release guarantees persistent enrichment of the photosensitizer inside tumor lesions throughout the entire TARE using ^{223}Ra-Chi/CaP-MB MS. Importantly, the gradually released MB can be effectively excited by Cerenkov photons, inducing robust CR-PDT-based tumor ablation.

In aqueous systems, ionizing radiations such as α-particles (produced by ^{223}Ra decay in this study), β-rays, and γ-rays trigger water radiolysis and produce ROS, which represents a key mechanism for ionizing radiation-mediated tumor cell killing [28, 29]. Meanwhile, Cerenkov radiation excites MB to initiate CR-PDT, which also yields ROS. Theoretically, benefiting from the additional CR-PDT pathway, ^{223}Ra-Chi/CaP-MB MS are expected to produce a greater quantity of ROS in aqueous solution relative to ^{223}Ra-Chi/CaP MS. To verify this, APF was utilized as a fluorescent probe to quantify ROS levels under distinct treatment groups. As presented in Fig. 2I, the APF fluorescence intensities of the ^{223}Ra-Chi/CaP MS and ^{223}Ra-Chi/CaP-MB MS groups were 1.25-fold and 1.86-fold higher than those of the blank control group, respectively. Notably, markedly stronger fluorescence signals were detected for the ^{223}Ra-Chi/CaP-MB MS group compared with the ^{223}Ra-Chi/CaP MS group. This observation confirms that CR further activates CR-PDT within MB-loaded microspheres, thereby amplifying overall ROS production.

In vitro antitumor activity of ^{223}Ra α-therapy combined CR-PDT

Prior to evaluating the *in vitro* tumoricidal effects of ^{223}Ra α-therapy and ^{223}Ra-mediated CR-PDT at the cellular level, we performed CCK-8 viability assays to screen suitable working concentrations of Chi/CaP MS, MB, and $^{223}RaCl_2$ for subsequent treatments by assessing their cytotoxicity toward rat N1S1 hepatoma cells. As summarized in **Fig. S5**, Chi/CaP MS displayed negligible cytotoxicity across the entire tested concentration range (0–2 mg/mL), with no apparent cell damage observed even at the maximum tested dose of 2 mg/L. These findings confirm that the Chi/CaP carrier itself exerts no overt adverse effects on N1S1 cells. Similarly, MB induced minimal cytotoxicity at concentrations ≤ 4 mg/L (Fig. 3A), whereas $^{223}RaCl_2$ caused no considerable cellular injury at doses below 1 μCi/mL. Notably,

moderate cytotoxicity occurred when cells were incubated with 2 μCi/mL $^{223}RaCl_2$, reducing the relative cell viability to 76.17% ± 3.40% (Fig. 3B). Accordingly, 4 mg/L of MB and 2 μCi/mL of $^{223}RaCl_2$ were selected for follow-up experiments to assess their combined synergistic antitumor activity.

Next, the *in vitro* antitumor efficacy of combined ^{223}Ra-mediated α-particle therapy and CR-PDT was evaluated under normoxic (O_2 concentration: 21%) and hypoxic (O_2 concentration: 1%) culture conditions. As shown in Fig. 3C, no obvious reduction in cell viability was observed for the MB group (96.34% ± 11.12%) under normoxia, whereas the ^{223}Ra-Chi/CaP MS group exhibited a cell viability of 76.19% ± 5.93%. Notably, ^{223}Ra-Chi/CaP-MB MS treatment markedly reduced cell viability to 57.63% ± 1.86%, verifying that ^{223}Ra-derived α-particles alone induce considerable cell death. Meanwhile, the combination of ^{223}Ra and MB activates CR-PDT, further augmenting therapeutic efficacy. In comparison, under hypoxic conditions, cell viability decreased to 85.96% ± 3.60% in the MB group and 63.35% ± 3.90% in the ^{223}Ra-Chi/CaP MS group, indicating that hypoxia itself elicits partial cell damage. Furthermore, ^{223}Ra-Chi/CaP-MB MS treatment produced a pronounced reduction in cell viability down to 44.45% ± 4.32%. These data demonstrate that ^{223}Ra can efficiently kill tumor cells even under hypoxic culture conditions, and robust activation of CR-PDT under hypoxia further facilitates tumor-cell killing. Collectively, these findings confirm that both ^{223}Ra-triggered cell killing and CR-PDT (a type-I PDT modality) exhibit oxygen-independent characteristics, enabling CR-PDT to produce potent synergistic antitumor effects with TARE against hypoxic solid tumors.

Furthermore, cell apoptosis assays and live/dead cell staining were performed to further evaluate the cytotoxic effects of ^{223}Ra-mediated α-particle therapy and CR-PDT under hypoxic conditions. As shown in Fig. 3D and **Fig. S6**, quantitative flow cytometry with Annexin V-FITC/PI double staining demonstrated that the ^{223}Ra-Chi/CaP-MB MS group exhibited an apoptosis rate of 23.45% ± 0.44%, which was markedly higher than that of the single-agent ^{223}Ra-Chi/CaP group (18.52% ± 0.20%). By contrast, MB treatment did not induce significant cell apoptosis (10.88% ± 0.24%, versus 9.89% ± 0.47% in the control group. Consistently, Calcein-AM/PI live/dead staining further verified the potent cell-killing efficacy upon treatment with ^{223}Ra-Chi/CaP-MB MS (Fig. 3E). The cytotoxicity induced by ^{223}Ra and CR-PDT fundamentally stems from the combined actions of high-LET α-particles and intracellular ROS, which cooperatively trigger DNA DSBs and subsequent apoptotic cell death. Accordingly, intracellular ROS levels were measured using the DCFH-DA fluorescent probe. As depicted in Fig. 3F and **Fig. S7**, the ^{223}Ra-Chi/CaP-MB MS group showed distinctly elevated ROS generation (52.64% ± 0.49%), which was significantly higher relative to the single-agent ^{223}Ra-Chi/CaP group (33.0% ± 0.27%). γ-H2AX immunofluorescence staining was conducted to evaluate DNA DSB damage. As illustrated in Fig. 3G, N1S1 cells in the ^{223}Ra-Chi/CaP-MB MS group exhibited more extensive DNA DSBs than cells treated with ^{223}Ra-Chi/CaP. These results confirm that α-particles emitted by ^{223}Ra can directly induce efficient DNA DSBs; meanwhile, α-particles initiate water radiolysis to generate ROS, and CR-PDT further amplifies

ROS production. Owing to these multi-modal effects, ^{223}Ra-Chi/CaP-MB MS treatment achieves robust tumor-cell killing even under hypoxic conditions.

Generally speaking, low-LET radiation (e.g., X-rays, γ-rays, and β-rays) exerts its biological effects predominantly through indirect effect: ionizing water molecules to generate ROS, which subsequently trigger DNA damage [30]. This process strongly depends on oxygen for damage “fixation”. As high-LET radiation, α-particles are also capable of producing ROS via water radiolysis. Nevertheless, their tumoricidal activity is dominated by the direct induction of DNA DSBs, an effect barely modulated by the oxygen partial pressure of the TME. Possessing an oxygen enhancement ratio (OER) close to or equal to 1, α-particles maintain potent cytotoxicity toward hypoxic tumor cells [11, 31]. For ^{223}Ra-Chi/CaP-MB MS-mediated tumor-cell killing, type-I CR-PDT similarly displays low-oxygen dependence. Accordingly, this combined system retains high efficiency in eliminating hepatoma cells under hypoxic culture conditions that recapitulate the *in vitro* TARE therapeutic scenario.

Apoptotic pathways triggered by combined α-particle therapy and CR-PDT

To explore the potential cell-killing mechanisms underlying ^{223}Ra-mediated α-particle therapy combined with CR-PDT, we performed RNA-seq analysis on ^{223}Ra-Chi/CaP-MB MS-treated and control N1S1 cells to screen and identify differentially expressed genes (DEGs) associated with the therapeutic pathways. Venn diagram analysis revealed that a total of 438 genes were specifically expressed in ^{223}Ra-Chi/CaP-MB group compared with the control group (Fig. 4A). Principal component analysis (PCA) clearly stratified all samples into two independent clusters, verifying substantial intergroup differences and distinct transcriptional profiles between the two groups (Fig. 4B). Using the criteria of $|\log_2$ fold change (FC)$| \geq 0.263$ and $P < 0.05$, volcano plot analysis identified 641 significantly altered DEGs in the ^{223}Ra-Chi/CaP-MB group, including 507 upregulated and 134 downregulated genes (Fig. 4C). Moreover, the clustered heatmap of DEGs visually confirmed the prominent transcriptional expression discrepancies between the ^{223}Ra-Chi/CaP-MB-treated group and the control group (**Fig. S8**). To further elucidate the functional implications of these DEGs, Gene Ontology (GO) analysis together with gene set enrichment analysis (GSEA) was performed to pinpoint signaling pathways perturbed upon ^{223}Ra-Chi/CaP-MB treatment. As illustrated in the bubble plot (Fig. 4D), multiple biological processes linked to DSB repair and cell-cycle regulation were significantly altered after ^{223}Ra-Chi/CaP-MB intervention. In line with these observations, GSEA revealed significant activation of cell-cycle-related pathways in the ^{223}Ra-Chi/CaP-MB group, with a normalized enrichment score (NES) > 0 and $P < 0.05$ (Fig. 4E). Notably, CDKN1A, a core negative regulator of cell-cycle progression that modulates cyclin-dependent kinase (CDK) activity and mediates cell-cycle arrest, was substantially upregulated in ^{223}Ra-Chi/CaP-MB MS-treated cells compared with controls (Fig. 4F). We further validated the cell-cycle-distribution changes predicted by transcriptomic profiling. As shown in Fig. 4G and 4H, the fraction of cells arrested at the G2/M phase was markedly higher in the ^{223}Ra-Chi/CaP-MB group than that in the control group (67.04% ± 5.47%

versus 11.63% ± 2.64%). Consistent with the RNA-seq data, western blot (Fig. 4I, J) and qRT-PCR assays (Fig. 4K) demonstrated that CDKN1A at both protein (3.7-fold) and mRNA (4.6-fold) levels were significantly elevated upon ^{223}Ra-Chi/CaP-MB treatment. It is reasonable to speculate that, ^{223}Ra-Chi/CaP-MB treatment upregulates CDKN1A to repress CDK1/CDK2 activities, consequently hindering the G2-to-M phase transition and triggering pronounced G2/M cell-cycle arrest.

Cell-cycle arrest, particularly G2/M-phase arrest, represents a vital defensive mechanism for cells responding to endogenous and exogenous stress, and also serves as a critical upstream event triggering apoptosis. Upon stimuli such as DNA damage and oxidative stress, cell-cycle checkpoints become activated to halt cell-cycle progression at specific phases and allow sufficient time for DNA repair. Nevertheless, when damage is excessively severe or arrest persists for prolonged periods, this cell-cycle block is converted into pro-apoptotic signals, ultimately driving cells toward programmed cell death [32, 33]. Thus, we propose the underlying antitumor mechanism of ^{223}Ra-Chi/CaP-MB therapy as follows: α-particles emitted by ^{223}Ra, together with excessive ROS produced by CR-PDT, induce severe DNA DSBs in N1S1 cells. Persistent DNA damage activates cellular DNA-damage checkpoint responses and markedly upregulates CDKN1A expression, which consequently halts cell-cycle progression and triggers G2/M-phase arrest. Owing to the overwhelming extent of DNA damage, injured N1S1 cells remain trapped in the G2/M phase for a prolonged period yet fail to complete DNA repair. Ultimately, unrepairable genomic lesions and sustained G2/M-phase arrest further initiate endogenous apoptosis, thereby conferring potent antitumor efficacy.

Performance of TARE in rat liver tumor models

The rat orthotopic N1S1 liver tumor model is a well-established animal model that closely mimics the pathological characteristics of HCC. Seven days after the establishment of orthotopic N1S1 tumor models, ^{18}F-FDG PET/CT imaging successfully identified focal intrahepatic hypodense lesions with robust radiotracer uptake (Fig. 5A). Quantitative analysis revealed that the SUVmax of tumor lesions was significantly higher than that of the surrounding normal liver parenchyma (1.653 ± 0.014 vs. 0.886 ± 0.052, $P < 0.05$; Fig. 5B). Gross morphological observation (Fig. 5C) and H&E histological staining (Fig. 5D) demonstrated distinct tumor boundaries and typical malignant histopathological features, corroborating the successful construction of rat orthotopic liver tumor models. Sustained intratumoral retention and minimal off-target accumulation are the prerequisites for radioactive-microsphere-based TARE against tumor. To systematically evaluate the intratumoral retention and *in vivo* biodistribution of ^{223}Ra-Chi/CaP-MB MS following TARE, sequential SPECT/CT imaging was performed at days 1, 5, 10, and 15 after intra-arterial injection in tumor-bearing rats (Fig. 5E). As illustrated in Fig. 5F, radioactive signals derived from ^{223}Ra-Chi/CaP-MB MS remained predominantly restricted to the tumor region throughout the entire observation period. Such durable, tumor-localized retention lays a solid foundation for effective TARE therapy. Quantitative biodistribution analysis revealed negligible radioactivity deposition in major extrahepatic organs, including lung, liver, heart, kidney, stomach, further confirming the favorable biosafety of TARE using ^{223}Ra-Chi/CaP-MB MS (Fig. 5G).

Clinically, the lung shunt fraction (LSF) is a critical clinical parameter during TARE for HCC, as hepatopulmonary shunting substantially influences dose prescription and constitutes a major dose-limiting factor for radioactive-microsphere therapy [34, 35]. Based on the estimated pulmonary radiation tolerance dose, the LSF is routinely incorporated into dosimetric calculations to determine the permissible injected activity of radioactive microspheres; excessive shunting of microspheres toward the pulmonary circulation may result in severe, potentially fatal radiation-induced lung injury, which renders pulmonary radiation dose an indispensable safety evaluation criterion before TARE administration. Once radioactive microspheres pass through arteriovenous shunts and lodge within pulmonary arterioles, irreversible radiation pneumonitis may develop months after treatment. In the present study, serial monitoring over 15 days following embolization with ^{223}Ra-Chi/CaP-MB MS demonstrated extremely low radiation exposure to the lungs in tumor-bearing rats. This favorable observation can be attributed to the high structural stability of these radioactive microspheres, which minimizes microsphere fragmentation and subsequent pulmonary translocation, and further guarantees the satisfactory *in vivo* biosafety of this therapeutic modality.

In vivo therapeutic efficacy of TARE using ^{223}Ra-Chi/CaP-MB MS

In the treatment experiment, tumor-bearing rats were randomly assigned to four groups: sham embolization, Chi/CaP MS, ^{223}Ra-Chi/CaP MS, and ^{223}Ra-Chi/CaP-MB MS groups. As shown in Fig. 6A–C, tumors in the sham embolization group exhibited continuous growth and progressively increased ^{18}F-FDG uptake throughout the observation period. Chi/CaP MS treatment moderately restrained tumor growth and attenuated tumor metabolic activity. In comparison, TARE using ^{223}Ra-Chi/CaP and ^{223}Ra-Chi/CaP-MB MS significantly reduced tumor SUVmax and exerted robust tumor growth suppression. Notably, the ^{223}Ra-Chi/CaP-MB MS group achieved markedly superior therapeutic outcomes relative to the ^{223}Ra-Chi/CaP MS group. Collectively, these results indicate that simple embolization therapy only yields limited tumor inhibitory effects and fails to eliminate tumor lesions. By contrast, α-particle-based TARE achieves obvious tumor eradication, and the introduction of CR-PDT further amplifies the overall antitumor efficacy of TARE, realizing a strengthened synergistic therapeutic effect.

Notably, embolization-triggered tumor hypoxia promotes compensatory neovascularization in HCC. The newly formed microvessels can supply oxygen and nutrients to residual tumor lesions, alleviate ischemic injury, sustain tumor viability, and eventually lead to insufficient therapeutic responses [36, 37]. Owing to the extremely short penetration range of α-particles, embolized ^{223}Ra-Chi/CaP-MB MS stably accumulate within the tumor vasculature, and efficiently eradicate perivascular hypoxic tumor cells while damaging vascular endothelial cells. This unique therapeutic effect potently suppresses embolization-provoked neovascularization and subsequent tumor revascularization. As shown in Fig. 6D, 6E, according to ^{68}Ga-DOTA-RGD PET/CT imaging, the Chi/CaP MS embolization group exhibited significantly higher intratumoral radiotracer uptake than the sham group on day 2 after treatment, confirming that simple embolization markedly promotes tumor neovascularization. In contrast, tumors treated with either ^{223}Ra-Chi/CaP MS or ^{223}Ra-Chi/CaP-MB MS showed distinctly reduced radiotracer accumulation, indicating

that α-particle-based TARE effectively inhibits tumor angiogenesis. Collectively, these findings demonstrate that high-LET α-particles emitted by ^{223}Ra severely disrupt tumor vascular architecture, efficiently abrogate hypoxia-induced compensatory neovascularization, and ultimately suppress tumor angiogenesis.

To further dissect the histological therapeutic responses and underlying mechanisms of ^{223}Ra-Chi/CaP-MB MS-mediated TARE, tumor tissues from all experimental groups were collected on day 15 post-treatment and subjected to H&E staining, TUNEL assay, and Ki-67 immunohistochemistry (Fig. 7A). H&E staining demonstrated large-scale necrotic areas in both the ^{223}Ra-Chi/CaP MS and ^{223}Ra-Chi/CaP-MB MS groups, with the most extensive tumor necrosis observed in the ^{223}Ra-Chi/CaP-MB group. Concordantly, TUNEL staining revealed the highest fraction of apoptotic tumor cells in the ^{223}Ra-Chi/CaP-MB group. Consistent with these findings, Ki-67 immunostaining showed marked inhibition of tumor-cell proliferation following ^{223}Ra-Chi/CaP-MB MS intervention. Collectively, these results corroborate that the combined actions of α-particle therapy and CR-PDT endow ^{223}Ra-Chi/CaP-MB MS-based TARE with superior antitumor therapeutic efficacy.

To further elucidate the regulatory effects of ^{223}Ra-Chi/CaP-MB MS-based TARE on tumor angiogenesis, immunofluorescence staining was conducted to detect three pivotal vascular biomarkers, including CD31, PDGFR-β, and CD105 [38]. CD31 is a canonical pan-endothelial marker that is widely utilized for the quantitative evaluation of tumor microvascular density. PDGFR-β acts as a specific pericyte biomarker, which indicates the maturity and structural stability of tumor vasculature. In contrast, CD105 is selectively expressed on neonatal endothelial cells and serves as a sensitive indicator for the activation and proliferation of tumor neovasculature. As illustrated in Fig. 7B and 7C, compared with control group, Chi/CaP MS embolization markedly upregulated CD31 and CD105 expression, indicating that severe intratumoral hypoxia triggered by embolization initiates compensatory tumor angiogenesis, which contributes to the limited therapeutic efficacy of embolization alone. Relative to the embolization-only group, the ^{223}Ra-Chi/CaP MS group displayed significantly reduced CD31 and CD105 levels. This suggests that α-particles effectively destroy vascular endothelial integrity and counteract hypoxia-driven compensatory angiogenesis, consequently restraining post-TARE tumor vascular remodeling. Additionally, further pronounced downregulation of CD31 and CD105 was detected in the ^{223}Ra-Chi/CaP-MB MS group. These results confirm that α-particle irradiation acts synergistically with CR-PDT-derived ROS to elicit severe vascular injury, maximally suppressing hypoxia-provoked compensatory tumor neovascularization.

Owing to the relatively low LET property of β-rays, conventional β-microspheres (e.g., ^{90}Y) still trigger hypoxia-induced neovascularization following TARE. VEGFA, the major pro-angiogenic factor that drives tumor angiogenesis, is up-regulated upon activation of hypoxia-stimulated pro-angiogenic pathways within the TME, and thus serves as a direct biomarker of compensatory tumor neovascularization [39]. As illustrated in **Fig. S9**, compared with control group, Chi/CaP MS embolization and TARE using ^{90}Y-MS both induced VEGFA upregulation, whereas TARE using ^{223}Ra-Chi/CaP MS or ^{223}Ra-Chi/CaP-MB MS

produced no significant change in VEGFA expression, demonstrating the potent anti-neovascularization activity of α-microspheres. These findings reveal that unlike β-microsphere-based TARE, which fosters tumor neovascularization, α-microsphere-based TARE strongly suppresses this process and produces therapeutic effects through a distinct mechanism from conventional β-microsphere.

Collectively, the superior therapeutic efficacy of ^{223}Ra-Chi/CaP-MB MS-based TARE against liver tumors can be attributed to three synergistic mechanisms. First, α-particle irradiation directly triggers the death of tumor cells, including hypoxic tumor cells residing around tumor vasculature. Second, this treatment potently inhibits pathological angiogenesis and post-embolization vascular remodeling. Third, MB-mediated CR-PDT further amplifies tumor cytotoxicity. This triple-modal therapeutic strategy enables ^{223}Ra-Chi/CaP-MB MS to synergistically improve the comprehensive therapeutic performance of TARE for liver tumor.

In vivo biosafety assessment of TARE with ^{223}Ra-Chi/CaP-MB MS

To systematically characterize the *in vivo* biosafety landscape of ^{223}Ra-Chi/CaP-MB MS-based TARE, we conducted routine hematology tests, longitudinal serum biochemical panels for hepatic and renal function, and histopathological examinations across all treatment groups. Routine hematological analysis identified no statistically significant deviations in primary hematologic parameters across all treatment arms (**Fig. S10**). On day 15 post-TARE, serum biomarkers of liver and renal function—including aspartate aminotransferase (AST), alanine aminotransferase (ALT), albumin (ALB), and blood urea nitrogen (BUN)—remained within standard physiological reference ranges, corroborating preserved hepatic albumin synthesis and intact glomerular filtration capacity (**Fig. S10**). H&E staining of vital organs revealed well-preserved tissue architectures without overt pathological lesions like inflammation or necrosis (**Fig. S11**). These cumulative toxicological findings confirm minimal off-target toxicity and the outstanding *in vivo* biosafety of TARE with ^{223}Ra-Chi/CaP-MB MS. Extensive preclinical studies on novel radioactive microspheres for TARE in HCC confirm that two key criteria govern the safety of this treatment: persistent microsphere retention within tumor vasculature and minimal radionuclide elution from the microsphere scaffold [8–10, 40, 41]. Post-TARE SPECT/CT imaging confirmed the long-term intratumoral retention and their robust structural stability of ^{223}Ra-Chi/CaP-MB MS, thereby contributing to the favorable safety profile of this therapeutic strategy.

Conclusion

Conventional TARE with β-emitting microspheres for HCC suffers compromised therapeutic efficacy due to embolism-induced intratumoral hypoxia, which confers robust radioresistance to tumor cells. In stark contrast, α-particles possess ultra-high LET and trigger oxygen-independent, irreparable clustered DNA DSBs, thereby eliciting robust cytotoxicity against hypoxic tumor subpopulations. Against this backdrop, we constructed a multifunctional α-emitting microsphere platform, designated ^{223}Ra-Chi/CaP-MB MS. This design integrates two complementary therapeutic mechanisms to achieve comprehensive tumor eradication. On one hand, localized α-irradiation effectively eliminates perivascular malignant lesions

(especially hypoxia-resistant tumor cells) while disrupting tumor vascular endothelium, thereby inducing profound tumor vessel ablation and suppressing compensatory angiogenic revascularization. On the other hand, Cerenkov photons continuously generated during ^{223}Ra decay chain trigger MB-mediated CR-PDT, which extends the therapeutic coverage to distant, avascular tumor foci that cannot be directly targeted by short-range α-particles. Benefiting from this dual-modal synergistic strategy, ^{223}Ra-Chi/CaP-MB MS-based TARE exerted robust tumor-suppressive efficacy in orthotopic rat liver tumor models. Combined with its favorable *in vivo* biosafety profile and potent tumoricidal activity, this novel α-emitting microsphere platform represents a transformative therapeutic strategy for HCC that is refractory to β-microsphere TARE.

Abbreviations

%ID/mL
Percentage injected dose per milliliter of tissue
^{131}I
Iodine-131
^{177}Lu
Lutetium-177
^{18}F-FDG
Fluorine-18 fluorodeoxyglucose
^{223}Ra
Radium-223
^{225}Ac
Actinium-225
^{68}Ga-DOTA-RGD
Gallium-68-labeled DOTA-conjugated Arg-Gly-Asp peptide
^{90}Y
Yttrium-90
ALB
Albumin
ALT
Alanine aminotransferase
ANOVA
Analysis of variance
APF
Aminophenyl fluorescein
AST
Aspartate aminotransferase
Ba

Barium
BET
Brunauer-Emmett-Teller
BJH
Barrett-Joyner-Halenda
BSA
Bovine serum albumin
BUN
Blood urea nitrogen
Calcein-AM
Calcein acetoxymethyl ester
CBC
Complete blood count
CCK-8
Cell counting kit-8
CD31
Cluster of differentiation 31
CD105
Cluster of differentiation 105 (endoglin)
CDK
Cyclin-dependent kinase
CDKN1A
Cyclin-dependent kinase inhibitor 1A
CHA
Common hepatic artery
Chi/CaP
Chitosan/calcium phosphate
CR
Cerenkov radiation
CR-PDT
Cerenkov radiation-induced photodynamic therapy
CT
Computed tomography
DAPI
4',6-diamidino-2-phenylindole
DCFH-DA
2',7'-dichlorodihydrofluorescein diacetate
DEGs
Differentially expressed genes
DMEM

Dulbecco's modified Eagle medium
DOTA
1,4,7,10-Tetraazacyclododecane-1,4,7,10-tetraacetic acid
DSBs
Double-strand breaks
DTG
Derivative thermogravimetry
ECL
Enhanced chemiluminescence
EDS
Energy-dispersive X-ray spectroscopy
FBS
Fetal bovine serum
FC
Fold change
FITC
Fluorescein isothiocyanate
FTIR
Fourier-transform infrared spectroscopy
GAPDH
Glyceraldehyde-3-phosphate dehydrogenase
GDA
Gastroduodenal artery
GO
Gene Ontology
GSEA
Gene set enrichment analysis
H&E
Hematoxylin and eosin
HCC
Hepatocellular carcinoma
HIF-1α
Hypoxia-inducible factor-1α
HRP
Horseradish peroxidase
HSD
Honestly significant difference
IHC
Immunohistochemistry
LET

Linear energy transfer
LSF
Lung shunt fraction
MB
Methylene blue
MS
Microspheres
NES
Normalized enrichment score
OER
Oxygen enhancement ratio
OSEM
Ordered-subset expectation maximization
PBS
Phosphate-buffered saline
PCA
Principal component analysis
PDGFR-β
Platelet-derived growth factor receptor β
PET
Positron emission tomography
PFA
Paraformaldehyde
PHA
Proper hepatic artery
PI
Propidium iodide
PVDF
Polyvinylidene difluoride
qRT-PCR
Quantitative real-time reverse transcription polymerase chain reaction
RGD
Arginine-glycine-aspartic acid
RIN
RNA integrity number
RIPA
Radioimmunoprecipitation assay
ROIs
Regions of interest
ROS

Reactive oxygen species
SD
Standard deviation
SDS-PAGE
Sodium dodecyl sulfate-polyacrylamide gel electrophoresis
SEM
Scanning electron microscopy
SPECT
Single-photon emission computed tomography
SPF
Specific pathogen-free
SSA
Specific surface area
SUVmax
Maximum standardized uptake value
TARE
Transarterial radioembolization
TBST
Tris-buffered saline with Tween-20
TG
Thermogravimetry
TGA
Thermogravimetric analysis
TME
Tumor microenvironment
TUNEL
TdT-mediated dUTP nick end labeling
UV–vis
Ultraviolet–visible
VEGFA
Vascular endothelial growth factor A
XRD
X-ray diffraction
γ-H2AX
Phosphorylated histone H2AX

Declarations

Ethics approval and consent to participate

All animal experiments were approved by the Animal Experiment Ethics Committee of Changhai Hospital, Naval Medical University (Approval No. CHEC (A.E) 2025-001, Programme No. 2025-016).

Competing interests

The authors declare no competing interests.

Author details

[1]Department of Nuclear Medicine, the First Affiliated Hospital of Naval Medical University, Shanghai 200433, China.

[2]Department of Radiology, Naval Medical Center, Shanghai 200433, China.

[3]School of Medical Imaging, Xuzhou Medical University, Xuzhou 221004, China.

[4]Shanghai Institute of Applied Physics, Chinese Academy of Sciences, Shanghai 201800, China.

[5]Institute of Hepatobiliary and Pancreatic Surgery, Department of Hepatobiliary and Pancreatic Surgery, Shanghai East Hospital, School of Medicine, Tongji University, Shanghai, 200120, China

Funding

This work was financially supported by the Major Research Plan of National Natural Science Foundation of China (Grant No. 92359204), National Natural Science Foundation of China (Grant No. 82272040, No. 82302247 and No. U25A20245) and the Strategic Priority Research Program of Chinese Academy of Sciences (Grant No. XDA0580000).

Author Contribution

Author contributionsWeiwei Su: Conceptualization, Investigation, Methodology, Formal analysis, Data curation, Writing-original draftQifan Xu: Conceptualization, Investigation, Methodology, Data curation, Writing-original draftYuqiao Wang: Investigation, Methodology, Data curation, Writing-original draftGuorong Jia: Methodology, ValidationTongyao Hu: Visualization, Data curationWenjie Li: MethodologyJiaojiao Li: ValidationJinming Tian: MethodologyChao Cheng: Validation, Dara curationYelin Wu: Conceptualization, Formal analysis, Supervision, Writing-review & editingXiao Li: Conceptualization, Formal analysis, Supervision, Writing-review & editingTao Wang: Conceptualization, Formal analysis, Project administration, Supervision, Writing-review & editingChangjing Zuo: Conceptualization, Formal analysis, Project administration, Supervision, Funding acquisition, Writing-review & editing

Acknowledgements

Not applicable.

Data Availability

All data generated or analysed during this study are included in this published article and its supplementary information files. The raw RNA sequencing data are available from the corresponding author on reasonable request.

References

1. Chan SL, Sun HC, Xu Y, Zeng H, El-Serag HB, Lee JM, et al. The Lancet Commission on addressing the global hepatocellular carcinoma burden: comprehensive strategies from prevention to treatment. Lancet. 2025;406:731–78.
2. Dhondt E, Lambert B, Hermie L, Huyck L, Vanlangenhove P, Geerts A, et al. ^{90}Y Radioembolization versus Drug-eluting Bead Chemoembolization for Unresectable Hepatocellular Carcinoma: Results from the TRACE Phase II Randomized Controlled Trial. Radiology. 2022;303:699–710.
3. Muglia R, De Giorgio M, Marra P, Carbone FS, Dulcetta L, Prussia C, et al. Long-term outcomes of Yttrium-90 transarterial radioembolization for patients with hepatocellular carcinoma. Eur J Nucl Med Mol Imaging. 2025;52:3114–24.
4. Kim M, Hui KM, Shi M, Reau N, Aloman C. Differential expression of hepatic cancer stemness and hypoxia markers in residual cancer after locoregional therapies for hepatocellular carcinoma. Hepatol Commun. 2022;6:3247–59.
5. Huynh KN, Rao S, Roth B, Bryan T, Fernando DM, Dayyani F, et al. Targeting Hypoxia-Inducible Factor-1alpha for the Management of Hepatocellular Carcinoma. Cancers (Basel). 2023;15:13.
6. Huang R, Zhou P-K. HIF-1 signaling: A key orchestrator of cancer radioresistance. Rad Med Prot. 2020;1:7–14.
7. Chu Q, Gu X, Zheng Q, Zhu H. Regulatory mechanism of HIF-1α and its role in liver diseases: a narrative review. Ann Transl Med. 2022;10:109.
8. Jia G, Wang T, Li R, Li X, Sun G, Chen W, et al. Radioiodine-131-Labeled Theranostic Nanoparticles for Transarterial Radioembolization and Chemoembolization Combination Therapy of VX2 Liver Tumor. Adv Healthc Mater. 2023;12:e2301559.
9. Jiang QR, Pu XQ, Deng CF, Wang W, Liu Z, Xie R, et al. Microfluidic Controllable Preparation of Iodine-131-Labeled Microspheres for Radioembolization Therapy of Liver Tumors. Adv Healthc Mater. 2023;12:e2300873.
10. Xiao L, Li Y, Geng R, Chen L, Yang P, Li M, et al. Polymer composite microspheres loading ^{177}Lu radionuclide for interventional radioembolization therapy and real-time SPECT imaging of hepatic

cancer. Biomater Res. 2023;27:110.

11. Wenker STM, van Lith SAM, Tamborino G, Konijnenberg MW, Bussink J, Heskamp S. The potential of targeted radionuclide therapy to treat hypoxic tumor cells. Nucl Med Biol. 2025; 140–1: 108971.
12. Russ E, Davis CM, Slaven JE, Bradfield DT, Selwyn RG, Day RM. Comparison of the Medical Uses and Cellular Effects of High and Low Linear Energy Transfer Radiation. Toxics. 2022; 10: 628.
13. Bertolet A, Ramos-Mendez J, Paganetti H, Schuemann J. The relation between microdosimetry and induction of direct damage to DNA by alpha particles. Phys Med Biol. 2021;66:155016.
14. Kairemo K. Targeted alpha therapy: a new tool for advanced prostate cancer. Lancet Oncol. 2024;25:148–49.
15. Song Z, Zhang J, Qin S, Luan X, Zhang H, Yang M, et al. Targeted alpha therapy: a comprehensive analysis of the biological effects from local-regional-systemic dimensions. Eur J Nucl Med Mol Imaging. 2025;53:30–47.
16. Yang H, Wilson JJ, Orvig C, Li Y, Wilbur DS, Ramogida CF, et al. Harnessing alpha-Emitting Radionuclides for Therapy: Radiolabeling Method Review. J Nucl Med. 2022;63:5–13.
17. Pratt EC, Shaffer TM, Bauer D, Lewis JS, Grimm J. Radiances of Cerenkov-Emitting Radionuclides on the In Vivo Imaging System. J Nucl Med. 2025;66:817–21.
18. Sun N, Wang T, Zhang S. Radionuclide-labelled nanoparticles for cancer combination therapy: a review. J Nanobiotechnol. 2024;22:728.
19. Wu MY, Huang SW, Kao IF, Yen SK. The Preparation and Characterization of Chitosan/Calcium Phosphate Composite Microspheres for Biomedical Applications. Polym (Basel). 2024; 16.
20. Chen H, Niu G, Wu H, Chen X. Clinical Application of Radiolabeled RGD Peptides for PET Imaging of Integrin alphavbeta3. Theranostics. 2016;6:78–92.
21. Xiang Q, Li D, Cheng C, Xu K, Zuo C. ^{68}Ga-HBED-CC-WL-12 PET in Diagnosing and Differentiating Pancreatic Cancers in Murine Models. Pharmaceuticals. 2023;16:80.
22. Tian J, Zhang Z, Cheng C, Yu F, Wang T, Cui B, et al. In-situ ^{223}Ra-doped calcium-alginate composite microspheres: a high-LET and immunoactivating platform for alpha-particle radioembolization in hepatocellular carcinoma. J Nanobiotechnol. 2026;24:114.
23. Akhmetova DR, Mitusova KA, Postovalova AS, Ivkina AS, Muslimov AR, Zyuzin MV, et al. Size-dependent therapeutic efficiency of ^{223}Ra-labeled calcium carbonate carriers for internal radionuclide therapy of breast cancer. Biomater Sci. 2024;12:453–67.
24. Su W, Wang H, Zhao S, Wang T, Hsu JC, Ji X, et al. Cerenkov radiation modulates the extracellular matrix for improved pancreatic cancer chemotherapy. Cell Biomater. 2026;2:100221.
25. Zhi L, Cheng C, Jing L, Zhi-Ping P, Lu Y, Yan T, et al. Application of fluorocarbon nanoparticles of ^{131}I-fulvestrant as a targeted radiation drug for endocrine therapy on human breast cancer. J Nanobiotechnol. 2024;22:107.
26. Chen YA, Li JJ, Lin SL, Lu CH, Chiu SJ, Jeng FS et al. Effect of Cerenkov Radiation-Induced Photodynamic Therapy with ^{18}F-FDG in an Intraperitoneal Xenograft Mouse Model of Ovarian

Cancer. Int J Mol Sci 2021; 22.
27. Lioret V, Bellaye PS, Arnould C, Collin B, Decreau RA. Dual Cherenkov Radiation-Induced Near-Infrared Luminescence Imaging and Photodynamic Therapy toward Tumor Resection. J Med Chem. 2020;63:9446–56.
28. Khazaei Monfared Y, Heidari P, Klempner SJ, Mahmood U, Parikh AR, Hong TS, et al. DNA Damage by Radiopharmaceuticals and Mechanisms of Cellular Repair. Pharmaceutics. 2023;15:2761.
29. Chen H, Han Z, Luo Q, Wang Y, Li Q, Zhou L, et al. Radiotherapy modulates tumor cell fate decisions: a review. Radiat Oncol. 2022;17:196.
30. Pouget JP, Mather SJ. General aspects of the cellular response to low- and high-LET radiation. Eur J Nucl Med. 2001;28:541–61.
31. Reissig F, Wunderlich G, Runge R, Freudenberg R, Luhr A, Kotzerke J. The effect of hypoxia on the induction of strand breaks in plasmid DNA by alpha-, beta- and Auger electron-emitters ^{223}Ra, ^{188}Re, ^{99m}Tc and DNA-binding ^{99m}Tc-labeled pyrene. Nucl Med Biol. 2020;80–81:65–70.
32. Wang Z. Cell Cycle Progression and Synchronization: An Overview. Methods Mol Biol. 2022;2579:3–23.
33. Otto T, Sicinski P. Cell cycle proteins as promising targets in cancer therapy. Nat Rev Cancer. 2017;17:93–115.
34. Sangro B, Martinez-Urbistondo D, Bester L, Bilbao JI, Coldwell DM, Flamen P, et al. Prevention and treatment of complications of selective internal radiation therapy: Expert guidance and systematic review. Hepatology. 2017;66:969–82.
35. Kappadath SC, Lopez BP, Salem R, Lam M. Reassessment of the lung dose limits for radioembolization. Nucl Med Commun. 2021;42:1064–75.
36. Pillai K, Ke K, Mekkawy A, Akhter J, Morris DL. Enhancement of treatment efficacy of hepatic tumours using Trans-arterial-chemoembolization. Am J Cancer Res. 2023;13:1623–39.
37. Pinto E, Pelizzaro F, Farinati F, Russo FP. Angiogenesis and Hepatocellular Carcinoma: From Molecular Mechanisms to Systemic Therapies. Med (Kaunas). 2023;59:1115.
38. Yao C, Wu S, Kong J, Sun Y, Bai Y, Zhu R, et al. Angiogenesis in hepatocellular carcinoma: mechanisms and anti-angiogenic therapies. Cancer Biol Med. 2023;20:25–43.
39. Viallard C, Larrivee B. Tumor angiogenesis and vascular normalization: alternative therapeutic targets. Angiogenesis. 2017;20:409–26.
40. Su XZ, Qiao EQ, Wu WY, Chen YR, Li Y, Song JH, et al. Radioprotectant-loaded visualizable cationic radioactive microspheres: Reduced hepatic tissue damage and intra/postoperative imaging during TARE. Mater Today Bio. 2026;37:102834.
41. Jiang X, Chen L, Xu X. Advancements in the investigation of radioactive microspheres for brachytherapy. Front Bioeng Biotechnol. 2025;13:1621418.

Figures

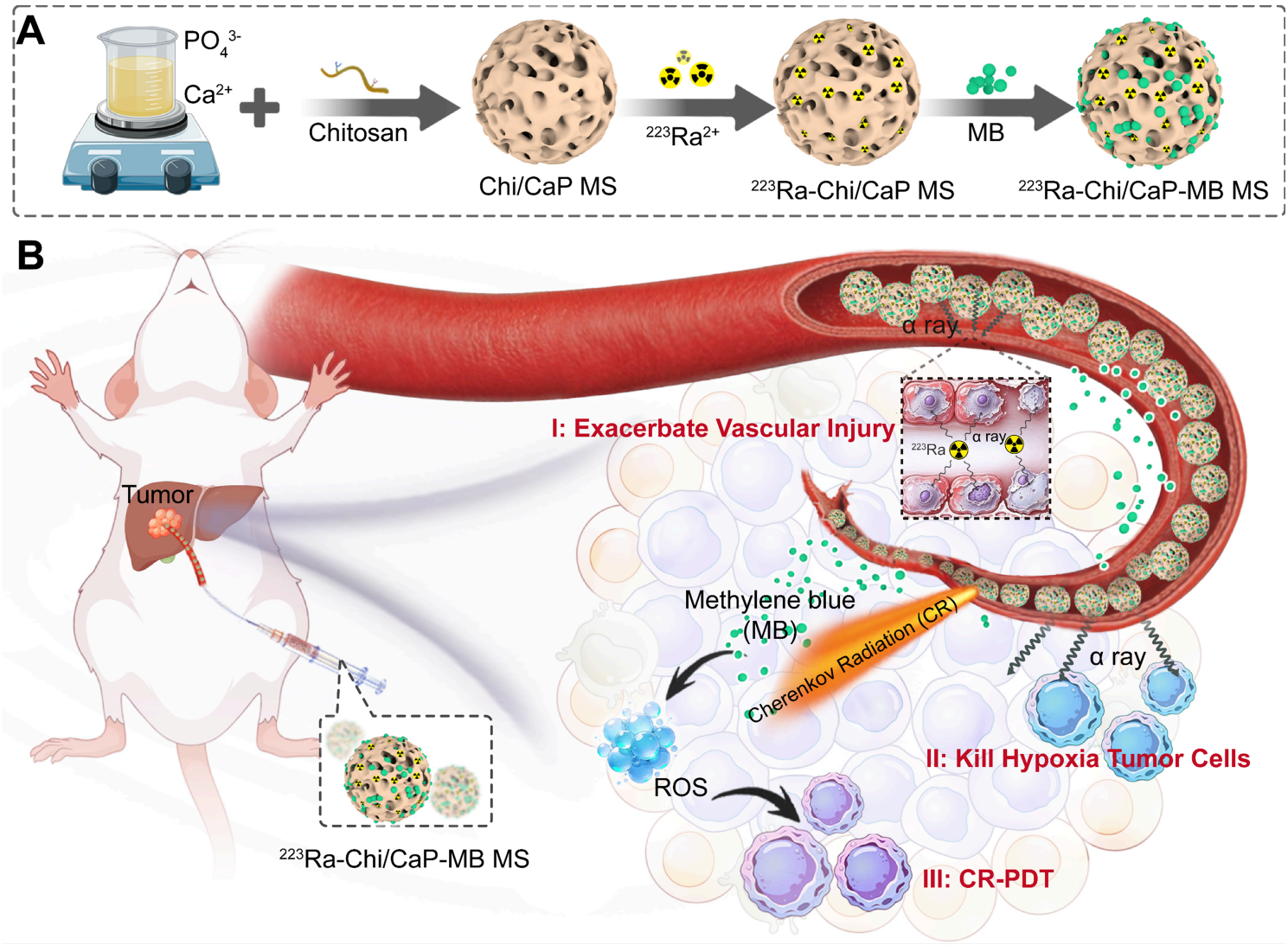


Figure 1

Synthesis of ^{223}Ra-Chi/CaP-MB microspheres and their application in TARE of liver tumor. (A) Schematic diagram of the synthesis process and structural characteristics of ^{223}Ra-Chi/CaP-MB microspheres. (B) Schematic of ^{223}Ra-Chi/CaP-MB microspheres enabling hypoxic tumor cell killing and vascular disruption, combined with CR-PDT to enhance TARE for liver cancer.

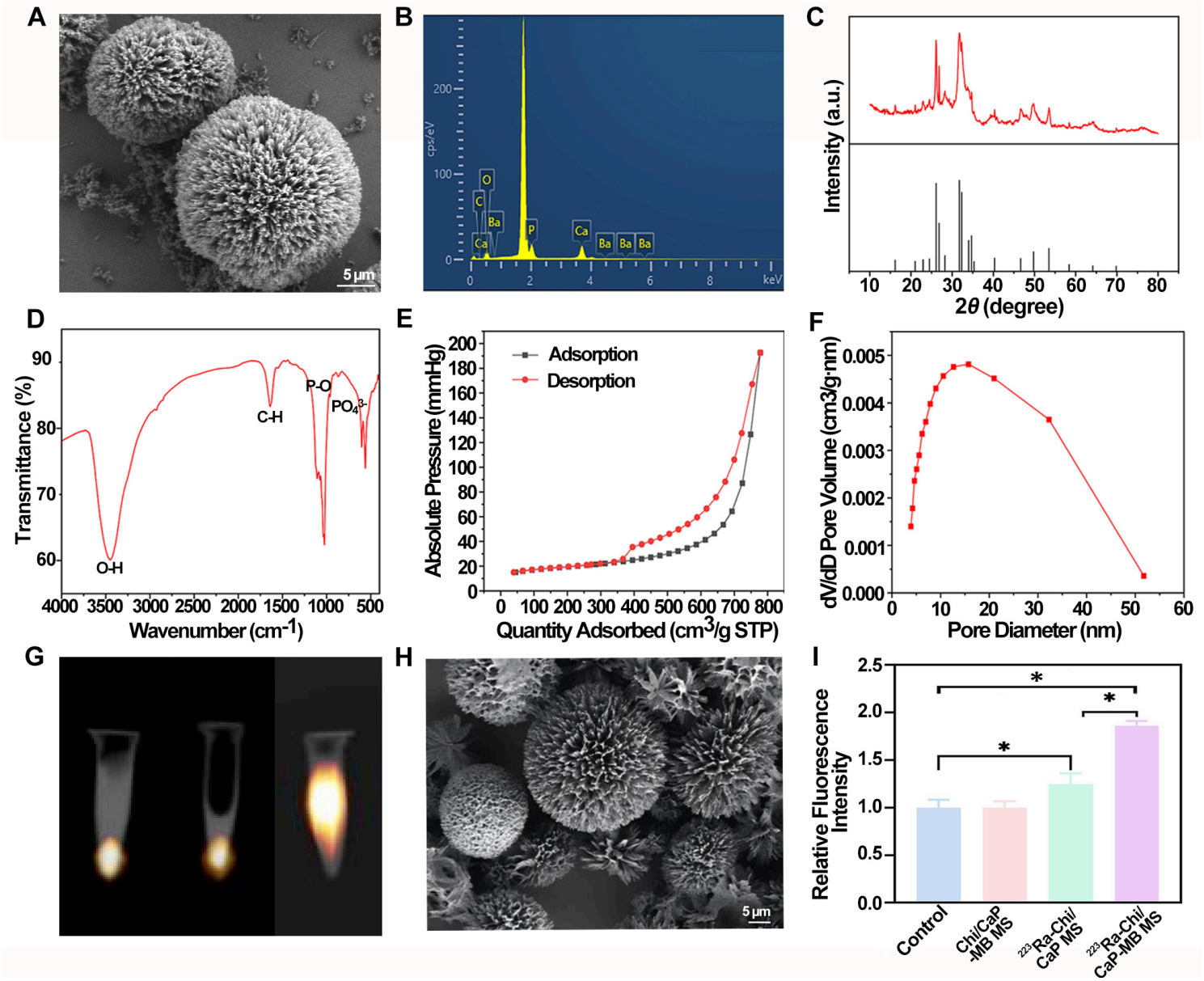


Figure 2

Synthesis and characterization of ^{223}Ra-Chi/CaP-MB MS. (A) SEM image of Chi/CaP MS. (B) EDS compositional analysis of Ba-Chi/CaP MS. (C) XRD patterns of Chi/CaP MS. (D) FTIR spectrum of Chi/CaP MS. (E) N_2 adsorption–desorption isotherms of Chi/CaP MS measured via the BET method. (F) The BJH pore-size distribution curve for Chi/CaP MS, calculated from the desorption branch of the nitrogen-desorption isotherm. (G) SPECT/CT images of ^{223}Ra-Chi/CaP MS (left), ^{223}Ra-Chi/CaP MS after 7 days of incubation in PBS (middle), and free $^{223}RaCl_2$ solution (right). (H) SEM image of ^{223}Ra-Chi/CaP MS following 50-day incubation in PBS. (I) ROS detection in aqueous Chi/CaP-MB, ^{223}Ra-Chi/CaP and ^{223}Ra-Chi/CaP-MB MS (n = 5, mean ± SD, *P < 0.05, one-way ANOVA followed by Tukey's test).

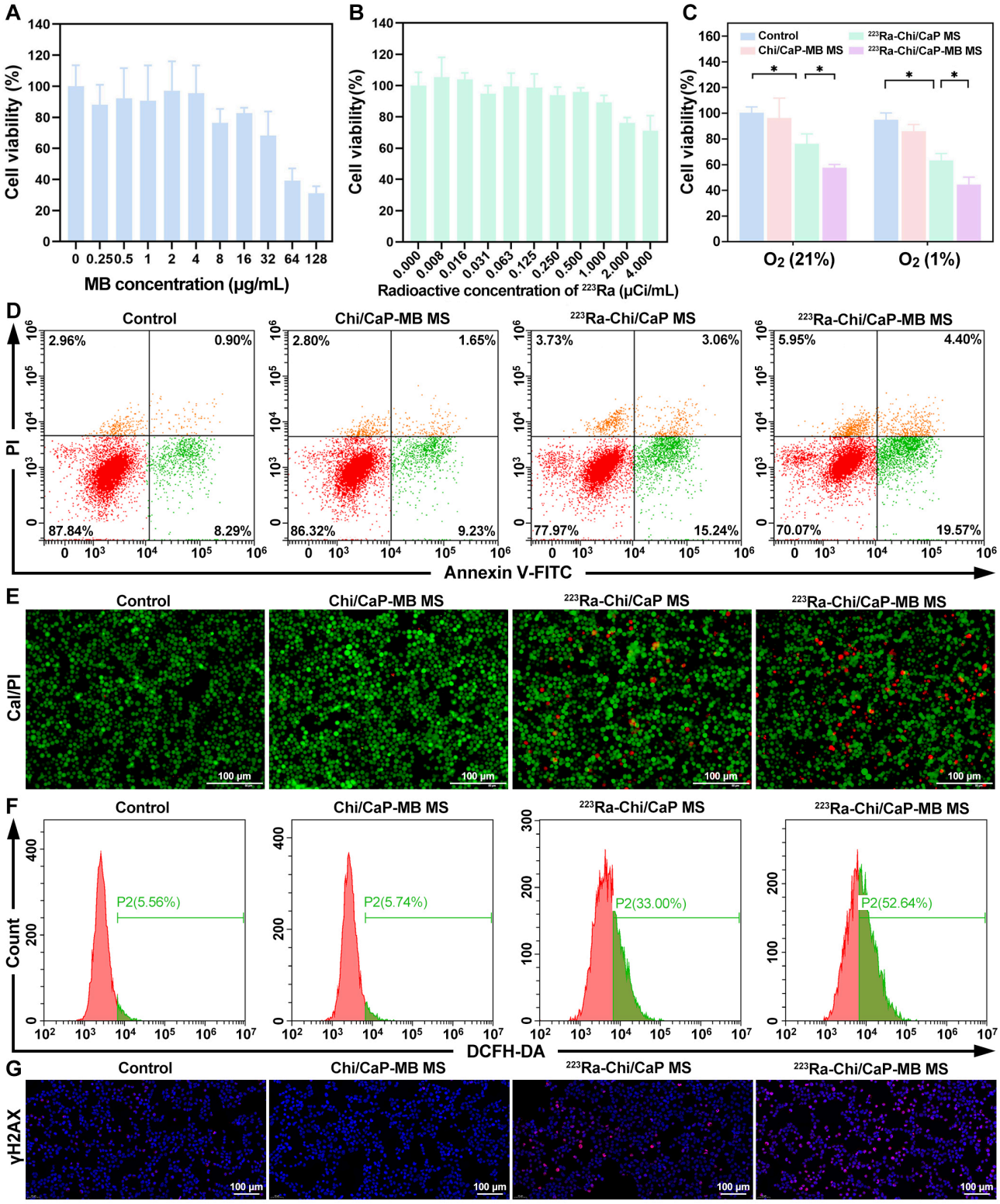


Figure 3

In vitro anti-tumor efficacy of combined ^{223}Ra-mediated α-particle therapy and CR-PDT. (A) The cytotoxicity of MB in N1S1 cells assessed by CCK-8 assay (n = 5, mean ± SD). (B) The cytotoxicity of $^{223}RaCl_2$ in N1S1 cells assessed by CCK-8 assay (n = 5, mean ± SD). (C) Cell viability of combined ^{223}Ra-based α-particle therapy and CR-PDT under normoxic and hypoxic conditions determined via CCK-8 assay (n = 5, mean ± SD, *P < 0.05, one-way ANOVA followed by Tukey's test). (D) Cell apoptosis

detection in different groups by flow cytometry. (E) Calcein-AM/PI live/dead cell staining for each treatment group (scale bar: 100 μm). (F) Intracellular ROS levels in different groups detected by flow cytometry. (G) Immunofluorescence staining of γ-H2AX for evaluating DNA DSBs in different groups (scale bar: 100 μm).

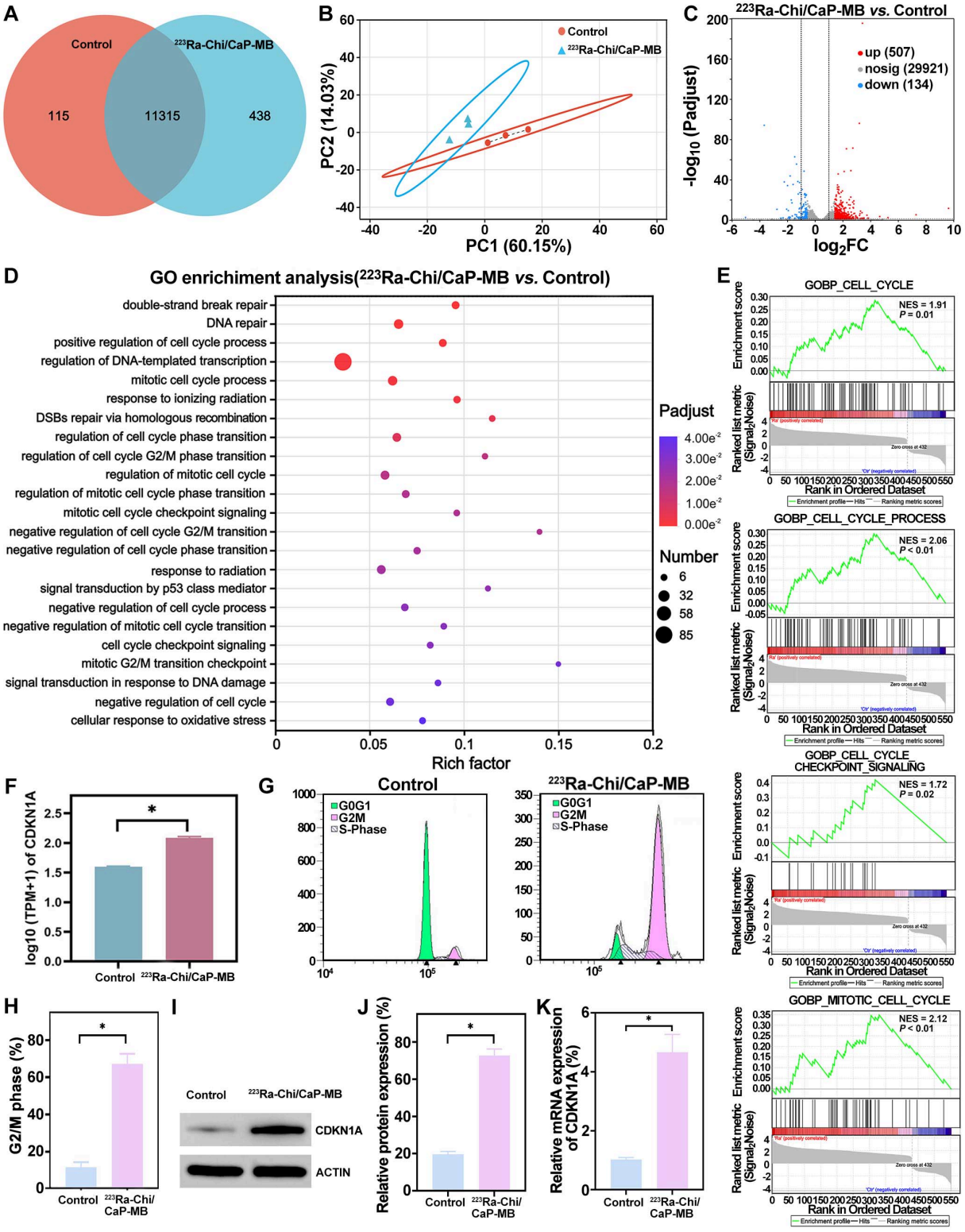


Figure 4

Potential cytotoxic mechanisms of ^{223}Ra-Chi/CaP-MB MS in N1S1 cells. (A) Venn diagram of DEGs in N1S1 cells treated with ^{223}Ra-Chi/CaP-MB and untreated (control) cells. (B) Principal component analysis of DEGs between the ^{223}Ra-Chi/CaP-MB group and the control group. (C) Volcano plot illustrating DEGs in N1S1 cells treated with ^{223}Ra-Chi/CaP-MB compared with control cells. (D) Bubble plot showing pathway enrichment analysis of DEGs between ^{223}Ra-Chi/CaP-MB MS-treated cells and control cells. (E) Gene Set Enrichment Analysis (GSEA) of cell cycle-related signaling pathways in N1S1 cells. (F) Expression levels of CDKN1A in cell samples from the ^{223}Ra-Chi/CaP-MB and control groups. (G) Cell cycle distribution in untreated control cells and ^{223}Ra-Chi/CaP-MB MS-treated cells. (H) Quantitative statistics of the proportion of cells in the G2/M phase in ^{223}Ra-Chi/CaP-MB and control groups (n = 3, mean ± SD, *P < 0.05, two independent samples t-test). (I) Western blotting analysis of CDKN1A protein expression in ^{223}Ra-Chi/CaP-MB MS-treated and control cells. (J) Quantitative analysis of CDKN1A protein expression levels (n = 3, mean ± SD, *P < 0.05, two independent samples t-test). (K) CDKN1A mRNA expression in N1S1 cells treated with ^{223}Ra-Chi/CaP-MB and control (n = 3, mean ± SD, *P < 0.05, two independent samples t-test).

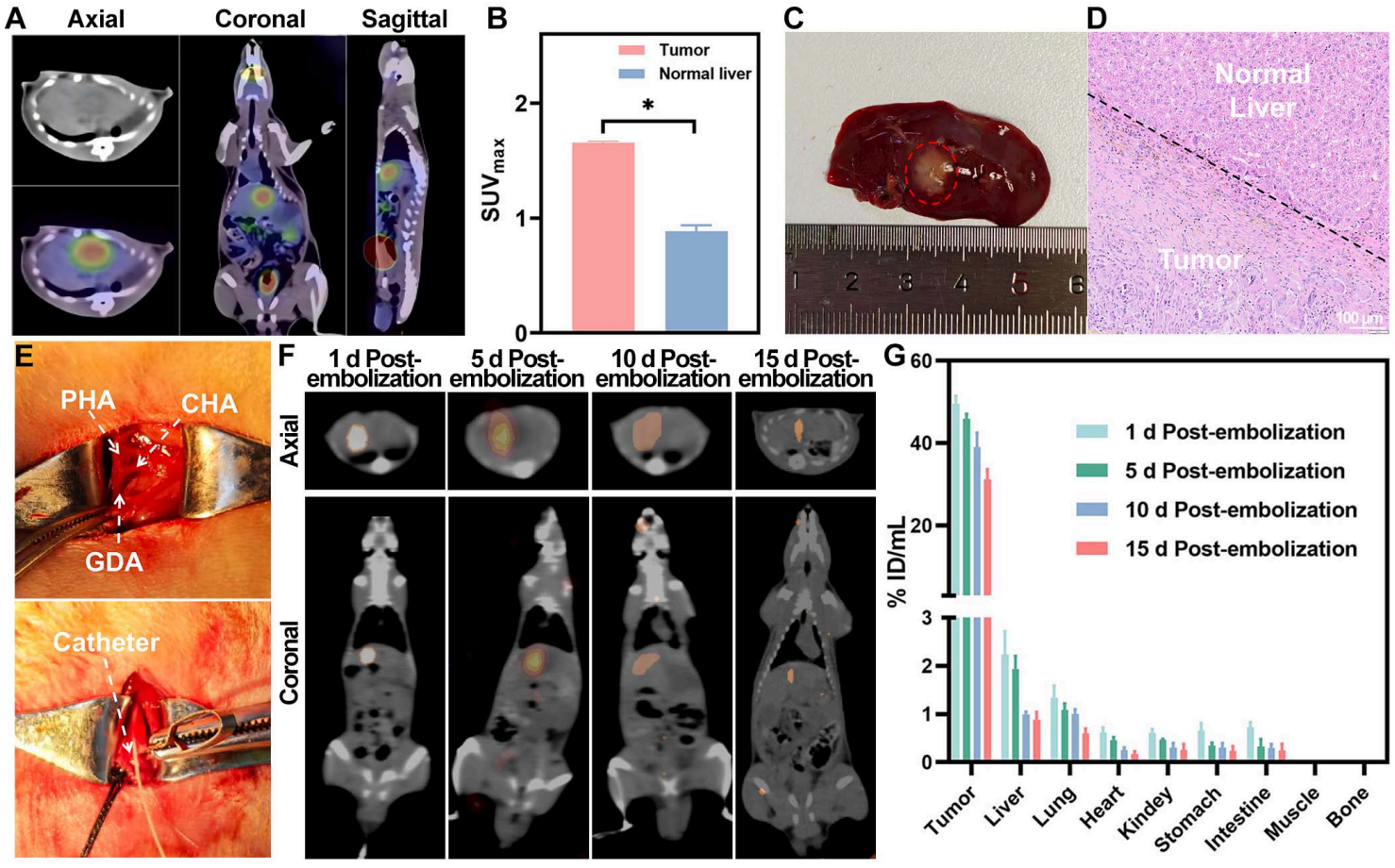


Figure 5

Tumor model establishment and biodistribution analysis of ^{223}Ra-Chi/CaP-MB MS following TARE treatment. (A) Representative ^{18}F-FDG PET/CT images of tumor-bearing rats. (B) Comparison of

SUVmax between tumor and normal liver tissue on PET/CT images (n = 5, mean ± SD, *P < 0.05). (C) Photograph of resected tumor-bearing liver specimens; tumor regions are outlined with red dotted lines. (D) H&E staining of normal liver and tumor tissue. Scale bars, 50 μm. (E) Intraoperative photographs of hepatic arterial catheterization. PHA, proper hepatic artery; CHA, common hepatic artery; GDA, gastroduodenal artery. (F) Serial ^{223}Ra SPECT/CT images acquired from day 1 to day 15 after intra-arterial injection of ^{223}Ra-Chi/CaP MS-MB. (G) Quantitative biodistribution of ^{223}Ra radioactivity in tumors and major organs over 15 days following administration of ^{223}Ra-Chi/CaP MS-MB (n = 3, mean ± SD), presented as percentage injected dose per milliliter (%ID/mL).

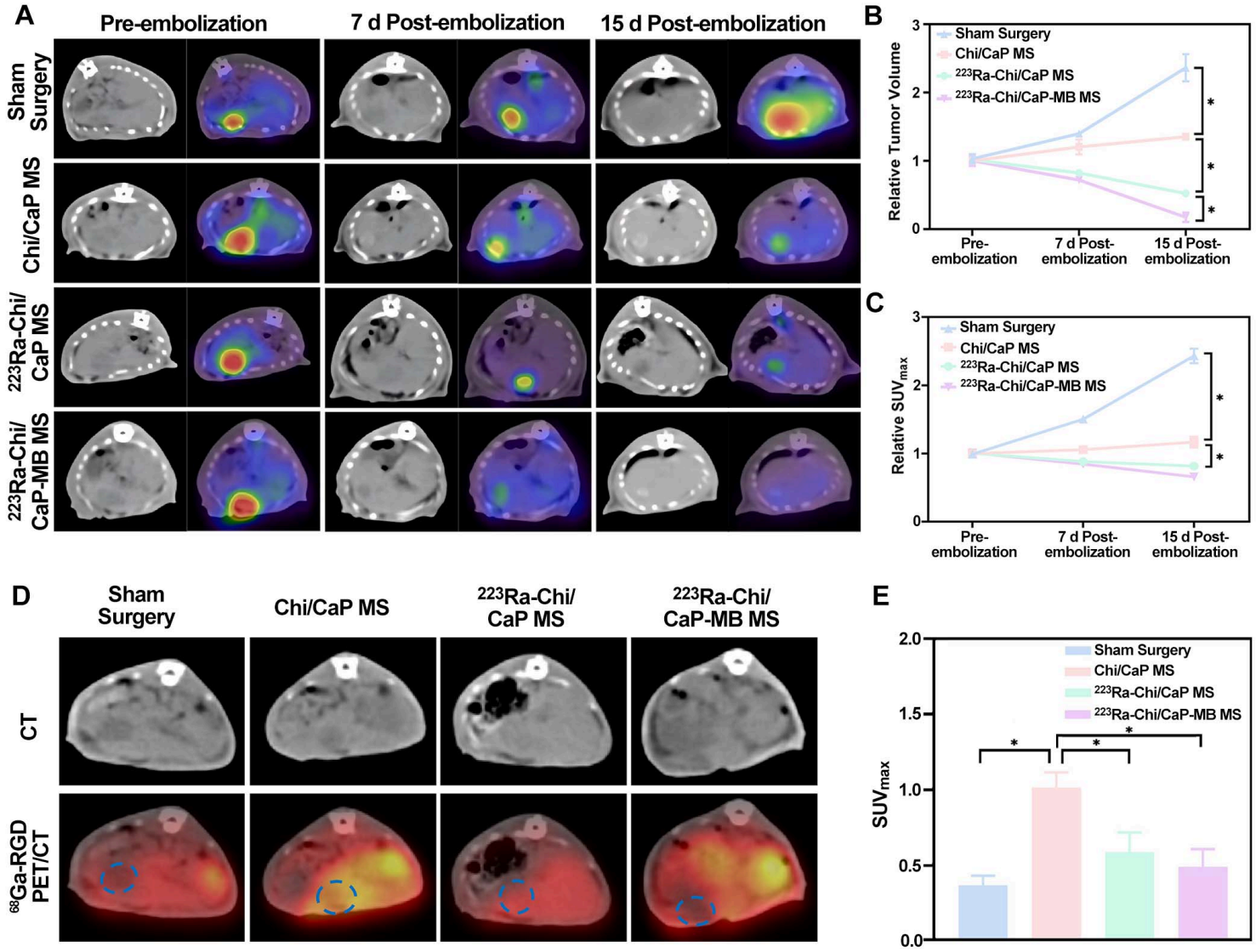


Figure 6

Evaluation of tumor growth, metabolism and neovascularization using PET/CT imaging. (A) Representative axial ^{18}F-FDG PET/CT fusion images and matched CT images acquired before embolization, and on days 7 and 15 post-treatment. (B) Longitudinal changes in tumor volume after different treatment (n = 3). (C) Longitudinal changes in tumor SUVmax after different treatment (n = 3). (D) Representative axial ^{68}Ga-DOTA-RGD PET/CT fusion images and matched CT images obtained 2

days after different treatment. (E) Comparison of tumor SUVmax among different groups on ^{68}Ga-DOTA-RGD PET/CT images (n = 3, mean ± SD, *P < 0.05, one-way ANOVA followed by Tukey's test).

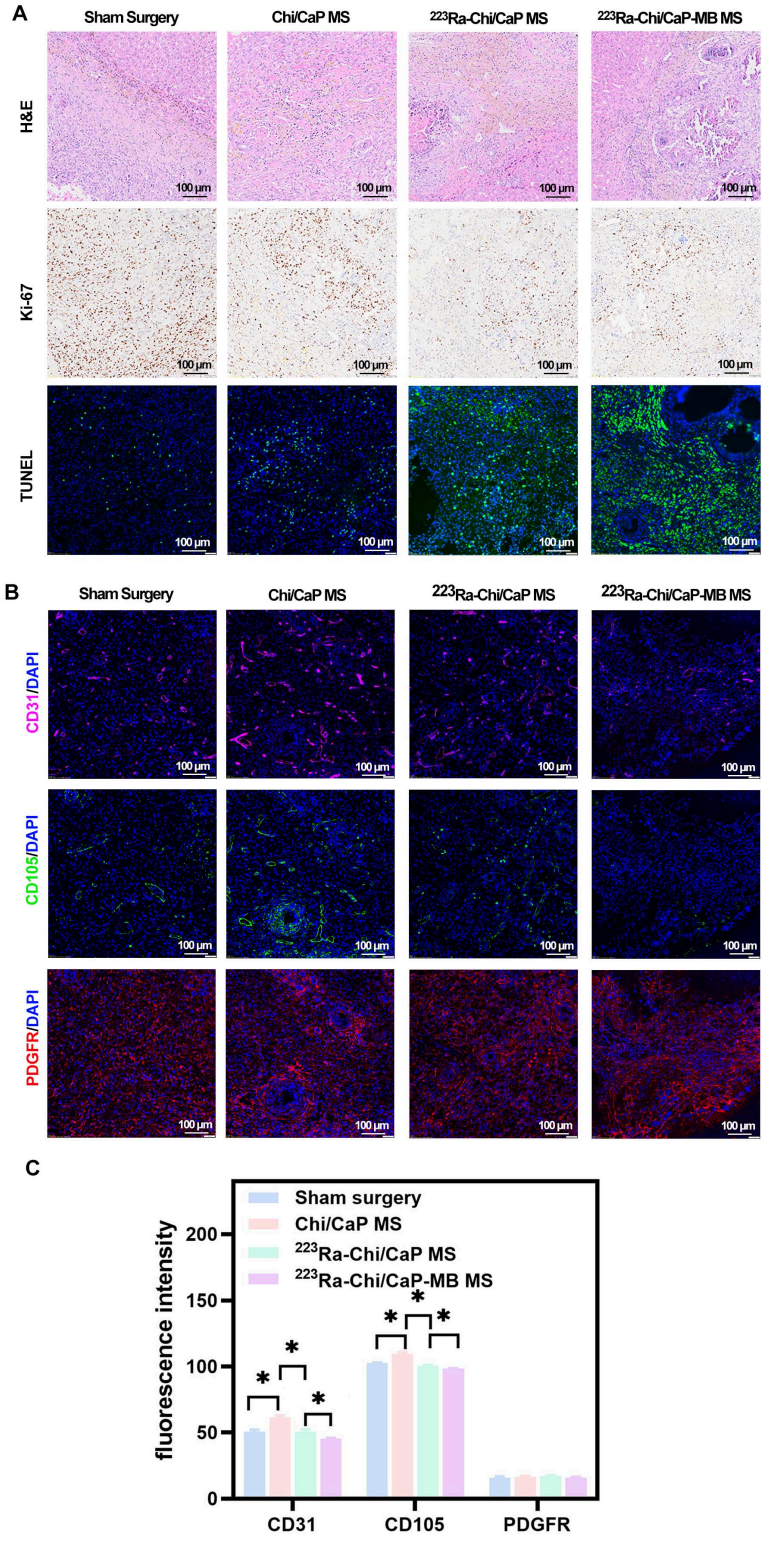


Figure 7

Histopathological and immunofluorescence analysis of tumor tissues following TARE treatment. (A) H&E staining, TUNEL assay, and Ki-67 immunohistochemistry (IHC) of tumor tissues. Scale bars, 100 μm. (B)

Immunofluorescence staining of CD31, PDGFR-β, and CD105 in tumor tissues. Scale bars, 100 μm. (C) Quantitative analysis of the expression levels of CD31, PDGFR-β, and CD105 in tumor tissues (n = 3, mean ± SD, *P < 0.05, one-way ANOVA followed by Tukey's test).

Supplementary Files

This is a list of supplementary files associated with this preprint. Click to download.

- Supplement.docx